

# AKARI NEAR-INFRARED SPECTROSCOPY OF LUMINOUS INFRARED GALAXIES

Jong Chul Lee<sup>1,2</sup>, Ho Seong Hwang<sup>3,4</sup>, Myung Gyoon Lee<sup>1</sup>, Minjin Kim<sup>2,5</sup>, and Joon Hyeop Lee<sup>2</sup>

<sup>1</sup> *Astronomy Program, Department of Physics and Astronomy, Seoul National University, Seoul 151-742, Republic of Korea; mglee@astro.snu.ac.kr*

<sup>2</sup> *Korea Astronomy and Space Science Institute, Daejeon 305-348, Republic of Korea; jclee@kasi.re.kr, mkim@kasi.re.kr, jhl@kasi.re.kr*

<sup>3</sup> *CEA Saclay/Service d'Astrophysique, F-91191 Gif-sur-Yvette, France*

<sup>4</sup> *Smithsonian Astrophysical Observatory, 60 Garden Street, Cambridge, MA 02138, USA; hhwang@cfa.harvard.edu*

<sup>5</sup> *National Radio Astronomy Observatory, 520 Edgemont Road, Charlottesville, VA, USA*

## ABSTRACT

We present the *AKARI* near-infrared (NIR; 2.5–5  $\mu\text{m}$ ) spectroscopic study of 36 (ultra)luminous infrared galaxies [(U)LIRGs] at  $z = 0.01 - 0.4$ . We measure the NIR spectral features including the strengths of 3.3  $\mu\text{m}$  polycyclic aromatic hydrocarbon (PAH) emission and hydrogen recombination lines ( $\text{Br}\alpha$  and  $\text{Br}\beta$ ), optical depths at 3.1 and 3.4  $\mu\text{m}$ , and NIR continuum slope. These spectral features are used to identify optically elusive, buried AGN. We find that half of the (U)LIRGs optically classified as non-Seyferts show AGN signatures in their NIR spectra. Using a combined sample of (U)LIRGs with NIR spectra in the literature, we measure the contribution of buried AGN to the infrared luminosity from the SED-fitting to the *IRAS* photometry. The contribution of these buried AGN to the infrared luminosity is 5–10%, smaller than the typical AGN contribution of (U)LIRGs including Seyfert galaxies (10–40%). We show that NIR continuum slopes correlate well with *WISE* [3.4]–[4.6] colors, which would be useful for identifying a large number of buried AGN using the *WISE* data.

*Subject headings:* galaxies: active – galaxies: ISM – galaxies: starburst – infrared: galaxies

## 1. INTRODUCTION

Since the *Infrared Astronomical Satellite* (*IRAS*; Neugebauer et al. 1984) first opened the all-sky view of far-infrared universe, a large number of luminous infrared galaxies (LIRGs;  $10^{11} \leq L_{\text{IR}}(8\text{--}1000 \mu\text{m}) < 10^{12} L_{\odot}$ ) and ultraluminous infrared galaxies (ULIRGs;  $L_{\text{IR}} \geq 10^{12} L_{\odot}$ ) have been identified and studied extensively (see Sanders & Mirabel 1996; Lonsdale et al. 2006; Soifer et al. 2008 for review).

In the local Universe, many of them are interacting systems between gas-rich disk galaxies [e.g., Kim et al. 2002; Veilleux et al. 2002; Wang et al. 2006; Kaviraj 2009; Hwang et al. 2010a; but see Elbaz et al. 2007; Lotz et al. 2008; Ideue et al. 2009; Kartaltepe et al. 2010, 2011 for high- $z$  (U)LIRGs]. They may evolve into quasars and then into intermediate-mass elliptical galaxies (e.g., Sanders et al. 1988a; Kormendy & Sanders 1992; Genzel et al. 2001; Tacconi et al. 2002; Dasyra et al. 2006; Veilleux et al. 2009b; Rothberg & Fischer 2010; Haan et al. 2011). Their enormous infrared luminosity comes from cool dust primarily heated by young stars [i.e., star formation (SF)] and hot dust heated by supermassive black holes (SMBHs) rapidly accreting matter [i.e., active galactic nuclei (AGN)]. Their contribution to the infrared luminosity density increases with redshift (e.g., Le Floc’h et al. 2005; Magnelli et al. 2009; Goto et al. 2011). Therefore, the study of (U)LIRGs allows us to better understand galaxy-galaxy interactions, starburst-AGN connection, and cosmic star formation history.

To identify the energy sources of galaxies (i.e., SF vs. AGN), the optical line ratios sensitive to the photoionization source have been used (e.g., Baldwin et al. 1981; Veilleux & Osterbrock 1987; Kewley et al. 2006). Based on this method, the optical spectral types for a large number of (U)LIRGs are also determined (e.g., Veilleux et al. 1995, 1999a; Kewley et al. 2001; Goto 2005; Cao et al. 2006; Hou et al. 2009; Lee et al. 2011). However, the optical spectral classification can be uncertain, in particular for (U)LIRGs, due to the difficulty of detecting dust-enshrouded AGN. In this case, near-infrared (NIR) spectroscopy, less affected by dust extinction, is a more efficient tool.

There are several ground-based  $K$ -band ( $1.9\text{--}2.4 \mu\text{m}$ ) spectroscopic surveys searching for obscured AGN signatures in (U)LIRGs: the presence of broad  $\text{Pa}\alpha$  emission centered at (rest-frame)  $1.875 \mu\text{m}$  or of high-excitation coronal line [Si VI] at  $1.963 \mu\text{m}$  (e.g., Veilleux et al. 1997, 1999b; Murphy et al. 1999, 2001). The ground-based  $L$ -band ( $2.8\text{--}4.2 \mu\text{m}$ ) spectroscopy was also used to constrain their energy source (e.g., Imanishi & Dudley 2000; Imanishi & Maloney 2003; Imanishi et al. 2006, 2011; Risaliti et al. 2006, 2010; Sani et al. 2008). The SF-dominated (U)LIRGs show a strong emission line at  $3.29 \mu\text{m}$  attributed to polycyclic aromatic hydrocarbons (PAHs), whereas AGN-dominated (U)LIRGs show a relatively PAH-free continuum attributed to larger-sized hot dust grains (e.g., Moorwood

1986; Imanishi & Dudley 2000). The strong absorption features at 3.05 and 3.4  $\mu\text{m}$  by  $\text{H}_2\text{O}$  ice-covered dust grains and bare carbonaceous dust, respectively, are found in (U)LIRGs with buried AGN. However, these absorptions are weak or absent in normal SF (U)LIRGs where energy sources and dust are often spatially well mixed (e.g., Imanishi & Dudley 2000; Imanishi & Maloney 2003). For a similar reason, NIR continua of AGN-dominated (U)LIRGs can be much redder than those of SF-dominated (U)LIRGs (e.g., Risaliti et al. 2006).

Thanks to the wide wavelength coverage (2.5–5  $\mu\text{m}$ ) and high sensitivity of the Infrared Camera (IRC) on-board the *AKARI* space telescope (Murakami et al. 2007; Onaka et al. 2007), the *L*-band diagnostic could be applied to more distant and faint galaxies (e.g., Imanishi et al. 2008, 2010a). The AGN detection rate from *L*-band spectroscopy appears to be larger than that from *K*-band spectroscopy (roughly 70% vs. 20% in ULIRGs) because the *K*-band diagnostic detects only obvious AGN. These NIR spectroscopic studies of (U)LIRGs suggest that there are many optically elusive buried AGN and that the buried AGN fraction increases with increasing infrared luminosity.

In this study, we analyze the *AKARI* NIR spectra of 36 (U)LIRGs<sup>1</sup> mainly from the cross-correlation between the *IRAS* and Sloan Digital Sky Survey (SDSS; York et al. 2000). Combining our new NIR spectroscopic data with those in Imanishi et al. (2008, 2010a), we investigate the NIR properties of a large sample of (U)LIRGs. The structure of this paper is as follows. The target selection is explained in Section 2. Observations and data reduction are described in Section 3, and the method of NIR spectral analysis is given in Section 4. Our findings are discussed and summarized in Sections 5 and 6, respectively. Throughout this paper, we adopt flat  $\Lambda$ CDM cosmological parameters:  $H_0 = 75 \text{ km s}^{-1} \text{ Mpc}^{-1}$ ,  $\Omega_M = 0.3$ , and  $\Omega_\Lambda = 0.7$ .

## 2. TARGETS

We obtained the *AKARI* NIR spectra of (U)LIRGs in three *AKARI* open-time programs: the nature of new ULIRGs at intermediate redshift (NULIZ), NIR spectroscopy of composite and LINER LIRGs (CLNSL), and NIR spectroscopy of star-forming infrared galaxies (NISIG). The main targets for the NULIZ program were selected from a catalog of  $\sim 320$  ULIRGs in Hwang et al. (2007), which was constructed by cross-correlating the *IRAS* faint source catalog (Moshir et al. 1992) with the galaxy redshift survey catalogs, including

---

<sup>1</sup>Although 5 out of 36 galaxies do not satisfy the definition of (U)LIRGs (i.e.,  $L_{\text{IR}} < 10^{11} L_\odot$ ), they are simply referred as (U)LIRGs in this study. We do not include them when we compare our results with those in previous studies.

the SDSS Data Release 4 (SDSS DR4; Adelman-McCarthy et al. 2006), 2dF Galaxy Redshift Survey (2dFGRS; Colless et al. 2001), and 6dF Galaxy Survey (6dFGS; Jones et al. 2004, 2005). These ULIRGs are detected up to  $z \sim 0.4$ . Because most ULIRGs observed with  $L$ -band spectrograph are at  $z < 0.2$ , we focus on 20 newly discovered ULIRGs at  $0.2 < z < 0.4$  to extend the NIR spectroscopy to intermediate- $z$  ULIRGs. The upper redshift limit ensures that the  $3.3 \mu\text{m}$  PAH emission falls within the AKARI spectral coverage. Additionally, four nearby ULIRGs were selected, as a control sample, from Soifer et al. (1989), Leech et al. (1994), Stanford et al. (2000), and Sanders et al. (2003).

For the CLNSL and NISIG programs, we first identified  $\sim 14,000$  infrared galaxies by the cross-correlation of infrared sources in the *IRAS* faint source catalog with the spectroscopic sample of galaxies in the SDSS DR7 (Abazajian et al. 2009; see Hwang et al. 2010a for more details). We selected  $\sim 13,000$  local infrared galaxies at  $0.01 < z < 0.2$ . We then determined their optical spectral types [star-forming, (SF-AGN) composite, low ionization nuclear emission-line region (LINER), and Seyfert 2] using their emission line fluxes based on the criteria of Kewley et al. (2006) (see Lee et al. 2011 for more details). The line flux measurements were drawn from the Max-Planck-Institute for Astrophysics/Johns Hopkins University value-added galaxy catalog<sup>2</sup> (MPA/JHU VAGCs; Kauffmann et al. 2003a; Tremonti et al. 2004; Brinchmann et al. 2004). We finally selected 60  $K_s$ -bright<sup>3</sup> non-Seyfert (i.e., SF, composite, and LINER) galaxies, covering a wide range of infrared luminosities ( $L_{\text{IR}} = 10^{10} - 10^{13} L_{\odot}$ ). Higher priority was assigned to  $K_s$ -bright galaxies in order to obtain high signal-to-noise ratio (S/N) *AKARI* spectra and to non-Seyfert galaxies in order to find “buried” AGN. Most targets are at high ecliptic latitudes due to the limited sky visibility of *AKARI* satellite (Sun-synchronous orbit; Murakami et al. 2007), but this does not introduce any bias to the results.

Among 48 observed targets, we use only 36 galaxies with median S/N per pixel for the continuum greater than three for the following analysis. Their basic information including the *IRAS* flux densities and optical spectral properties is summarized in Table 1. We plot the infrared luminosity versus redshift of our sample in Figure 1. The (U)LIRGs in Imanishi et al. (2008, 2010a), hereafter the Imanishi sample<sup>4</sup>, are also plotted for comparison. The two samples are overall in a similar range of infrared luminosities, while our sample

---

<sup>2</sup><http://www.mpa-garching.mpg.de/SDSS/DR7/>

<sup>3</sup> $K_s$ -band ( $2.17 \mu\text{m}$ ) 20 mag arcsec<sup>-2</sup> isophotal ellipse aperture magnitude drawn from the 2 micron all-sky survey (2MASS)  $< 14.5$  mag

<sup>4</sup> This sample contains ULIRGs from the *IRAS* 1 Jy sample (Kim & Sanders 1998) and LIRGs from the bright galaxy sample (BGS; Soifer et al. 1987; Sanders et al. 1995) and from the revised BGS (Sanders et al. 2003).

is more numerous than the Imanishi sample at  $0.2 < z < 0.4$ . Imanishi et al. also preferentially selected non-Seyfert (U)LIRGs. In the result, non-Seyfert fractions in these samples are large compared to the fractions among their parent samples (from  $\sim 55\%$  to  $\sim 70\%$  in ULIRGs and from  $\sim 65\%$  to  $\sim 80\%$  in LIRGs).

### 3. OBSERVATIONS AND DATA REDUCTION

We observed the target galaxies with the IRC spectrograph (Onaka et al. 2007) on-board the *AKARI* satellite. It is a slitless spectroscopy, but the targets are located inside a  $1 \times 1$  arcmin<sup>2</sup> window in order to avoid the spectral overlap with nearby sources. The 2.5–5  $\mu$ m wavelength range was covered at a spectral resolution of  $R \sim 120$  ( $\sim 2500$  km s<sup>−1</sup>) with NG grism. In the observing modes, the total on-source exposure time per pointing is about six minutes, and the  $3\sigma$  detection limit is roughly 0.6 mJy. Each target was observed one to eight times (mostly twice), depending on its visibility and on  $K_s$ -band magnitude. The observation log is given in Table 2. Note that the NULIZ data were obtained in Phase 2 cooled by liquid helium, while the CLNSL and NISIG data were obtained in Phase 3 cooled by a cryocooler.

Data reduction was carried out using the IDL packages prepared by the *AKARI* team: “IRC Spectroscopy Toolkit Version 20101025” for the NULIZ data and “IRC Spectroscopy Toolkit for Phase 3 data Version 20101025” for the CLNSL and NISIG data. Both packages are available online<sup>5</sup>. This involves dark subtraction, linearity correction, flat-fielding, sub-frame combining, source detection, background subtraction and source extraction, wavelength calibration, and flux calibration. Because one pointing consists of eight (or nine) sub-frames, cosmic rays are efficiently removed. The wavelength calibration accuracy is  $\sim 0.01$   $\mu$ m ( $\sim 1$  pixel). The absolute flux calibration accuracy is  $\sim 10\%$  at the central wavelength and can be larger than 20% at the edge (Ohyama et al. 2007).

We derived the spatial profile of each source in the two-dimensional spectra obtained with the slitless spectrograph. To extract one-dimensional spectra, we used 3–9 pixels ( $3\text{--}9 \times 1''.46$ ) along the spatial direction. The aperture width (see column 2 in Table 3) was determined to contain signals larger than the background noise level, which is the root-mean-square (rms) of fluxes at each side 11–15 pixel away from the center of the source. Since the aperture is large enough to cover the NIR emission even for extended sources, no aperture correction is applied. For the sources observed several times, the spectra were stacked by taking the median. The data collected during the late part of Phase 3 of *AKARI*

---

<sup>5</sup> <http://www.ir.isas.jaxa.jp/ASTRO-F/Observation/DataReduction/IRC/>

are sometimes seriously affected by bad pixels and background noise because of the increase of the temperature in IRC. If there were some data sets substantially inferior to others, they were not used to obtain the final spectra.

We display the final spectra of 36 (U)LIRGs with the continuum  $S/N > 3$  in Figure 2. These spectra show various continuum shapes, ranging from steeply decreasing ones to nearly flat ones with increasing wavelength. In most spectra, the PAH emission feature at  $3.29 \mu\text{m}$  is clearly seen.  $\text{Br}\alpha$  ( $2.63 \mu\text{m}$ ) and  $\text{Br}\alpha$  ( $4.05 \mu\text{m}$ ) hydrogen recombination lines and broad absorption features from  $\text{H}_2\text{O}$  ice ( $3.05 \mu\text{m}$ ) and bare carbonaceous dust ( $3.4 \mu\text{m}$ ) are detected in some cases.

#### 4. MEASUREMENTS

Figure 3 shows an example of spectral fitting to the NIR spectrum. We fit each emission line of the  $\text{Br}\alpha$ ,  $\text{Br}\beta$ , and  $3.3 \mu\text{m}$  PAH with a single Gaussian function after subtracting the local continuum defined by a linear fit around the line. Especially for the  $3.3 \mu\text{m}$  PAH profile, we choose an asymmetric fitting range ( $3.15\text{--}3.35 \mu\text{m}$ ) in order to avoid contamination of the  $3.4 \mu\text{m}$  sub-peak (see Imanishi et al. 2010a). We compute the equivalent width of the PAH emission using the fitted Gaussian profile on top of the global continuum (see next paragraph). By using the global continuum instead of the local continuum, we can reduce the effect of adjacent absorption feature on the equivalent width measurement. We set an upper limit for the non-detection by assuming that the line has a Gaussian profile with a full width at half maximum (FWHM) and with an amplitude twice the local rms of the continuum-subtracted spectrum. As for the fixed FWHMs, we use the typical values measured from the *AKARI* spectra in this study:  $2500 \text{ km s}^{-1}$  for the Bracket lines and  $4000 \text{ km s}^{-1}$  for the PAH feature. The linewidth of the Bracket lines is well matched to the instrumental resolution. The linewidth of the PAH feature is consistent with the PAH profile in other studies (e.g., type-1 sources in Tokunaga et al. 1991).

The global continuum slope  $\Gamma$  is determined using a single power-law model ( $F_\lambda \propto \lambda^\Gamma$ ) with data points less-affected by line features in the observed wavelengths at  $2.7\text{--}4.8 \mu\text{m}$ . The data points near the edge of the spectra are excluded because of their large flux uncertainty (Ohyama et al. 2007). The optical depths of the  $3.1$  and  $3.4 \mu\text{m}$  dust absorption features ( $\tau_{3.1}$  and  $\tau_{3.4}$ , respectively) are calculated as the natural logarithmic ratios between the adopted continuum levels and the observed absorption profiles. The continuum levels are adopted from the global continuum, and the absorption profiles are obtained after smoothing the spectrum with a 10 pixel box ( $\sim 0.1 \mu\text{m}$ ) to minimize noise effect. We consider that the absorption feature is detected when the maximum difference between the continuum level

and the absorption profile is twice larger than the local rms.

Measurements are listed in Table 3. The uncertainties estimated by considering the local rms values are also listed. The median S/Ns of detected features are 6.4, 5.2, 3.6, 3.3, and 3.1 for  $3.3\ \mu\text{m}$  PAH,  $\text{Br}\alpha$ ,  $\text{Br}\beta$  fluxes,  $\tau_{3.1}$ , and  $\tau_{3.4}$ , respectively. We present the equivalent width of  $3.3\ \mu\text{m}$  PAH emission line ( $\text{EW}_{3.3\text{PAH}}$ ) versus continuum slope ( $\Gamma$ ) diagram in Figure 4. It shows that most (U)LIRGs have  $\text{EW}_{3.3\text{PAH}} < 150\ \text{nm}$  and  $-3 < \Gamma < 0$ ; the distribution of our sample is not different from that of the Imanishi sample.

## 5. RESULTS AND DISCUSSION

### 5.1. AGN Diagnostics

#### 5.1.1. AGN signature in the NIR spectra

Emission at  $3.3\ \mu\text{m}$  is a prominent feature in (U)LIRG NIR spectra. It probably originates from the reprocessing of ultraviolet (UV) radiation by PAH molecules. The contribution of  $\text{P}\delta$  emission line at a similar wavelength is usually negligible. If (U)LIRGs host AGN, the  $\text{EW}_{3.3\text{PAH}}$  is suppressed because hot dust emission from the AGN increases the NIR continuum flux level and X-ray photons may destroy PAH molecules (e.g., Smith et al. 2007). A red NIR continuum (i.e., a high value of continuum slope) as well as strong absorption features at  $3.1$  and  $3.4\ \mu\text{m}$  from  $\text{H}_2\text{O}$  ice-covered dust grains inside molecular clouds and bare carbonaceous dust in the diffuse interstellar medium, respectively (see Draine 2003), indicate the presence of highly obscured compact sources. While many of these absorbed sources with red continuum slopes have been shown to harbor buried AGN (e.g., Risaliti et al. 2006; Sani et al. 2008; Imanishi et al. 2010a), deeply buried starbursts can also produce the same spectral signatures (e.g., Desai et al. 2007; Spoon et al. 2007; Veilleux et al. 2009a) and in general all that is required is a warm, highly obscured heating source. The small PAH equivalent width condition is useful for identifying weakly obscured AGN, while the large continuum slope and optical depth conditions are efficient in detecting highly obscured AGN. Therefore, all of these diagnostics are necessary to detect as many obscured AGN as possible.

Following the criteria in Imanishi et al. (2010a), we regard  $\text{EW}_{3.3\text{PAH}} < 40\ \text{nm}$ ,  $\Gamma$  ( $F_\lambda \propto \lambda^\Gamma$ )  $> -1$ ,  $\tau_{3.1} > 0.3$ , and  $\tau_{3.4} > 0.2$  as AGN signatures, and classify sources satisfying at least one of these conditions as NIR AGN-detected galaxies (see column 10 in Table 3). In the results, we find 19 AGN out of 36 (U)LIRGs based on these criteria. Among these AGN, there are 13 sources with  $\text{EW}_{3.3\text{PAH}} < 40\ \text{nm}$  (68%), five sources with  $\Gamma > -1$  (26%), five sources with  $\tau_{3.1} > 0.3$  (26%), and three sources with  $\tau_{3.4} > 0.2$  (16%). Note that

some sources satisfy more than one criterion. Therefore,  $\text{EW}_{3.3\text{PAH}} < 40$  nm is the primary criterion to select AGN. A similar trend is also seen in the Imanishi sample (56, 43, 45, and 10% for  $\text{EW}_{3.3\text{PAH}}$ ,  $\Gamma$ ,  $\tau_{3.1}$ , and  $\tau_{3.4}$ , respectively).

We count the number of sources with AGN signatures among our sample (U)LIRGs in bins of optical spectral type and of infrared luminosity. These results are summarized in Table 4 together with those from the Imanishi sample. The NIR AGN detection rates for our sample and the Imanishi sample are on average 53% and 51%, respectively, and agree well in each bin. Imanishi et al. (2008, 2010a) found that the AGN signature in NIR spectra is more often detected in optical AGN-like and in more luminous infrared galaxies. Our sample appears to follow these trends, as shown in Figure 5. However, it is not conclusive with our data alone because of large uncertainties, in particular, for the NIR AGN detection rate depending on optical spectral type. In the combined sample of 180 (U)LIRGs with  $L_{\text{IR}} \geq 10^{11} L_{\odot}$ , the NIR AGN detection rate depends on optical spectral type as follows: 36% for SF (U)LIRGs, 55% for composite (U)LIRGs, and 66% for Seyfert 2 (U)LIRGs. Note that most of previously classified LINERs are called composites in this study because we adopted the selection criteria of Kewley et al. (2006) rather than those of Veilleux & Osterbrock (1987) that were used in Imanishi et al. (2008, 2010a). There are two Seyfert 1 (U)LIRGs in the combined sample, and both of them show AGN signatures in their NIR spectra. The total NIR AGN detection rates for LIRGs and ULIRGs are 29% and 65%, respectively. If we select (U)LIRGs without any priority to non-Seyfert galaxies, the NIR AGN detection rates for (U)LIRGs increase slightly [e.g., 30% for LIRGs and 70% for ULIRGs based on the (U)LIRG sample in Yuan et al. (2010)].

When we consider non-Seyfert galaxies with AGN signature in the NIR to be optically elusive buried AGN, the buried AGN fraction (i.e., the number ratio of buried AGN to non-Seyferts) increases with infrared luminosity: 24% for (U)LIRGs with  $L_{\text{IR}} = 10^{11} - 10^{12} L_{\odot}$ , 60% for (U)LIRGs with  $L_{\text{IR}} = 10^{12} - 10^{12.3} L_{\odot}$ , and 84% for (U)LIRGs with  $L_{\text{IR}} = 10^{12.3} - 10^{13} L_{\odot}$ . The higher AGN fraction in more luminous infrared galaxies has been reported in previous studies based on the data from not only *AKARI* but also the *Infrared Space Observatory (ISO)*; e.g., Lutz et al. 1998; Rigopoulou et al. 1999; Tran et al. 2001) and *Spitzer Space Telescope* (e.g., Desai et al. 2007; Imanishi 2009; Valiante et al. 2009; Veilleux et al. 2009a; Petric et al. 2011), suggesting an important role of AGN in increasing infrared luminosity.

As expected, we find many non-Seyfert (U)LIRGs with AGN signatures in their NIR spectra [buried AGN; 49% (55/113)]. On the other hand, a substantial number of Seyfert (U)LIRGs do not show the AGN signatures in the NIR [33% (14/43)]. The apertures used in the optical spectroscopy (our sample: 3" diameter fiber; Imanishi sample: 2" wide slit and 2 kpc extraction) are smaller than those of NIR spectroscopy (covers the entire galaxy



size). The line measurements in the optical spectra for our sample are aperture-corrected following the method in Hopkins et al. (2003), but those for the Imanishi sample are not. The small aperture used for the optical spectral classification may miss the extended emission associated with star formation, and hence be more sensitive to weak, central AGN. This helps to understand the existence of Seyferts without AGN signatures in the NIR. We find no difference in the redshift distribution between Seyferts with and without AGN signatures in the NIR spectra. The different aperture size between the optical and NIR spectroscopy seems partially responsible for the disagreement of spectral types.

Regardless of the aperture effect, if the hot dust emission from AGN is very weak because of a tiny covering of dust around the AGN, such AGN are clearly visible in the optical spectrum. However, they would be not distinguishable from SF-dominated galaxies based on the NIR diagnostics (see Nardini et al. 2010). In contrast, when AGN are really heavily obscured, both optical and NIR diagnostics are less powerful. Then the observations at other wavelengths are necessary to detect them (e.g., X-ray: Bauer et al. 2010; Teng & Veilleux 2010; mid/far-infrared: Farrah et al. 2007; Spoon et al. 2007; Veilleux et al. 2009a; Hatziminaoglou et al. 2010; Elbaz et al. 2011; but see also Elbaz et al. 2010; Hwang et al. 2010b; radio: Sajina et al. 2008; Imanishi et al. 2010b).

In Figure 6, we present the optical AGN diagnostic diagram based on  $[\text{OIII}]\lambda 5007/\text{H}\beta$  and  $[\text{NII}]\lambda 6584/\text{H}\alpha$  line ratios, and NIR AGN diagnostic diagram based on  $\text{EW}_{3.3\text{PAH}}$  and continuum slope. In panel (a), the optical AGN (Seyfert+LINER) without the NIR AGN signature have low  $[\text{OIII}]/\text{H}\beta$  ratios compared to those with AGN signatures both in optical and in NIR spectra. On the other hand, in panel (b), the NIR properties of optical AGN without the NIR AGN signature are not significantly different from those of non-AGN both in optical and in NIR spectra.

### 5.1.2. AGN contribution to the infrared luminosity

To measure the contribution of buried AGN to the infrared energy budget of (U)LIRGs, we use the infrared spectral energy distribution (SED) templates and fitting routine of Mullaney et al. (2011), DECOMPIR<sup>6</sup>. These templates consist of one AGN and five host-galaxy SEDs. For the host-galaxy SEDs, *Spitzer* mid-infrared spectra of starburst galaxies are extrapolated to the far-infrared using *IRAS* photometry. These host-galaxy SEDs are grouped into five categories, referred to as ‘SB1’ through ‘SB5’, in terms of their overall shape and relative strength of PAH features. For the AGN SED, the intrinsic SEDs of

---

<sup>6</sup><http://sites.google.com/site/decompir>

AGN-dominated sources are derived after subtracting suitable host-galaxy components from the observed SEDs, and these SEDs are averaged. The infrared SEDs of AGN show a large spread, mainly dependent on dust distribution around AGN (i.e., smooth vs. clumpy torus structures). However, the different AGN SEDs do not significantly change the resulting AGN contribution to the infrared luminosity in (U)LIRGs (see Mullaney et al. 2011; Pozzi et al. 2012). Based on this SED fitting with sparse photometric data points such as *IRAS*, Mullaney et al. (2011) found that the intrinsic AGN luminosities measured are actually correlated with those from high-resolution mid-infrared observations of the AGN cores.

We apply this routine to 69 (U)LIRGs with  $S/Ns > 3$  at all four *IRAS* bands (12, 25, 60, and 100  $\mu m$ ) in the combined sample, and fit their SEDs five times with AGN and one of host-galaxies by allowing renormalization of these two templates. We choose the best-fit solution with the lowest  $\chi^2$  value, computing the AGN contribution to the infrared (8–1000  $\mu m$ ) luminosity from this template set. Figure 7 represents example SEDs with the best-fit AGN and host-galaxy templates. The AGN contribution in (U)LIRGs ranges from 0% to 69%, and is on average 6–8% in LIRGs and 11–19% in ULIRGs. Because the combined sample preferentially includes non-Seyferts, the AGN contribution in this study seems to be small compared to other studies (e.g., LIRGs:  $\sim 10\%$  in Petric et al. 2011; ULIRGs:  $\sim 20\%$  in Farrah et al. 2003; 35–40% in Veilleux et al. 2009a;  $\sim 25\%$  in Nardini et al. 2010; 15–20% in Risaliti et al. 2010).

Figure 8 shows the correlation of the AGN contribution with the presence of AGN signature in the NIR, optical spectral type, and infrared luminosity. Not surprisingly, the AGN contribution is higher in (U)LIRGs with AGN signature in the NIR than in those without AGN signature. The AGN contribution clearly increases with increasing infrared luminosity (see also Donoso et al. 2012), similar to the trend of buried AGN fraction in Figure 5 (b). The AGN contribution for Seyfert (U)LIRGs is slightly larger than those for SF and composite (U)LIRGs.

### 5.1.3. AGN diagnostics with *WISE* data

Recently, the *Wide-field Infrared Survey Explorer* (*WISE*; Wright et al. 2010) opens up the opportunity to probe mid-infrared properties (3.4, 4.6, 12, and 22  $\mu m$ ) for a large sample of galaxies with excellent sensitivity. We use the *WISE* all-sky survey source catalog<sup>7</sup> to identify the *WISE* counterparts of the (U)LIRGs observed with *AKARI* IRC and (U)LIRGs

---

<sup>7</sup> <http://wise2.ipac.caltech.edu/docs/release/allsky/>

at  $0.01 < z < 0.4$  in the SDSS DR7 (Hwang et al. 2010a) within  $3''$ .

In Figure 9 (a), we compare the continuum slope  $\Gamma$  with *WISE* [3.4]–[4.6] color (Vega magnitude system; Jarrett et al. 2011) for the *AKARI* (U)LIRGs. We overplot the expected *WISE* [3.4]–[4.6] colors from simple power-law continuum models as a function of continuum slope (solid line). The continuum slope  $\Gamma$  and *WISE* [3.4]–[4.6] color show a tight correlation (Spearman rank correlation coefficient = 0.82; the probability of obtaining the correlation by chance =  $1.03 \times 10^{-30}$ ) with some offset and scatter around the expected relation. Most sources have small values of continuum slope compared to the expectation because the presented slopes (fitting range:  $2.7\text{--}4.8\ \mu\text{m}$ ) are affected by the spectrum at  $<3.4\ \mu\text{m}$  where the stellar population contribution is large (see Lee et al. 2010). The scatter may come from the contamination by the  $3.3\ \mu\text{m}$  PAH feature. For the galaxies at  $z < 0.13$ , the presence of  $3.3\ \mu\text{m}$  PAH emission makes [3.4]–[4.6] color bluer than the color without the PAH emission. On the other hand, if the galaxies are at  $0.26 < z < 0.55$ , the presence of  $3.3\ \mu\text{m}$  PAH emission makes [3.4]–[4.6] color redder than the color without the PAH emission. The amount of change in colors depends on redshift and on the strength of PAH emission. From the experiment with the spectra of our sample, we find that the presence of PAH emission can change the [3.4]–[4.6] color by  $\pm 0.2$  mag, consistent with the scatter in Figure 9 (a).

We find that the AGN selection criterion based on the continuum slope (i.e.,  $\Gamma > -1$ ) in this study is roughly equivalent to that of [3.4]–[4.6]  $> 0.8$  suggested by Stern et al. (2012) (see also Assef et al. 2010; Jarrett et al. 2011). If (U)LIRGs with AGN signatures in the NIR spectra are regarded as genuine AGN (filled symbols), the *WISE* color criterion selects AGN with 72% completeness (51 out of 71 genuine AGN satisfy the *WISE* color criterion) and 76% reliability (51 out of 67 objects which satisfy the *WISE* color criterion are genuine AGN).

Figure 9 (b) shows the *WISE* [3.4]–[4.6] colors versus *IRAS* flux density ratios between 25 and  $60\ \mu\text{m}$  (hereafter *IRAS* 25– $60\ \mu\text{m}$  colors) for the SDSS (U)LIRG sample. The *IRAS* 25– $60\ \mu\text{m}$  color is known to be associated with nuclei activity in infrared-luminous galaxies (e.g., de Grijp et al. 1985; Sanders et al. 1988b; Neff & Hutchings 1992; Veilleux et al. 2009a; Lee et al. 2011). AGN-dominated galaxies show warm *IRAS* 25– $60\ \mu\text{m}$  colors ( $f_{25}/f_{60} \geq 0.2$ ), while SF-dominated galaxies show cool colors ( $f_{25}/f_{60} < 0.2$ ). The composite and SF galaxies show similar distributions in this domain, but the AGN are significantly different. The median colors of AGN differ from those of non-AGN with significance levels of  $6.8\sigma$  and  $7.4\sigma$  in the *IRAS* and *WISE*, respectively. Interestingly, there are a substantial number of SF (U)LIRGs in the lower-right corner. It seems real even if we consider large uncertainties associated with the *IRAS* colors. They have warm dust emission without hot dust emission, therefore appearing to be heavily obscured AGN. As a result, the *WISE* [3.4]–[4.6] color is

a good tracer of AGN-heated hot dust emission, but may not be sufficient to detect heavily obscured AGN.

## 5.2. Comparison between Optical and Infrared Properties

### 5.2.1. Star formation rate indicators

The total infrared continuum, 3.3  $\mu\text{m}$  PAH emission, and recombination lines including  $\text{H}\alpha$  and  $\text{Br}\alpha$  of galaxies are useful indicators of star formation rate (SFR) (Kennicutt 1998). In Figure 10 (a–b), we compare these SFR indicators: infrared luminosity versus (a)  $\text{H}\alpha$  and (b) 3.3  $\mu\text{m}$  PAH luminosities. The  $\text{H}\alpha$  luminosities are extinction-corrected using the Balmer decrement and Calzetti et al. (2000) extinction curve. The expected relationships are overplotted between these parameters (dotted lines; hereafter SF galaxy sequences):  $L_{\text{H}\alpha}/L_{\text{IR}} = 10^{-2.25}$  from the empirical relation in Kennicutt (1998) and  $L_{3.3\text{PAH}}/L_{\text{IR}} = 10^{-3}$  from the observations of Mouri et al. (1990) and Imanishi (2002). These panels show that there are large offsets and scatters between the data and the expected relationships, even for SF (U)LIRGs without any AGN signature [pure SF (U)LIRGs; large filled symbols]. The offset from the SF galaxy sequence is larger in ULIRGs than in LIRGs, suggesting that  $\text{H}\alpha$  and 3.3  $\mu\text{m}$  PAH emissions are more depressed in ULIRGs.

There could be several reasons for the strong depression of  $\text{H}\alpha$  and 3.3  $\mu\text{m}$  PAH emission in ULIRGs. (1) The amount of dust extinction could be systematically underestimated in ULIRGs. To check this effect, we plot the observed line ratios of  $\text{Br}\alpha/\text{H}\alpha$  and  $\text{H}\alpha/\text{H}\beta$  in panel (c). The pure SF (U)LIRGs appear to have larger  $\text{Br}\alpha/\text{H}\alpha$  ratios by considering the extinction curve of Calzetti et al. (2000) with a typical  $R_V$  value of 4.05. This can imply the need of a larger  $R_V$  value for the extinction correction in (U)LIRGs [e.g.,  $R_V = 5.01$  denoted by the arrow]. Some studies also suggest the need of flatter/grayer extinction curves (i.e., large  $R_V$  values) in ULIRGs, which may be attributed to supernovae-driven large-size dust grains (e.g., Kawara et al. 2011; Shimizu et al. 2011; see also Boquien et al. 2012). However, because of large scatter in the data and different aperture size between the optical and NIR spectroscopy, it should be checked with a more extensive data set in future studies. (2) Even for ULIRGs without any AGN signature in optical and NIR observations, there could still be hidden AGN that play a role in the relative depression of line emission. To remove contamination of hidden AGN, it is necessary to search for AGN at other wavelengths. However, it is expected that the contribution of buried AGN is not significant as discussed in Section 5.1.2. (3) The line emission from ULIRGs may be intrinsically weak. Regardless of the presence of AGN, the star formation in ULIRGs produces large infrared continuum emission because a larger fraction of stellar UV photons is absorbed by dust

inside star-forming regions under the strong radiation field in ULIRGs (Abel et al. 2009). The PAH emission in ULIRGs may be depressed in the sense that intense radiation fields do not produce photo-dissociation regions that are necessary for PAH emission, or lead to the destruction of PAH carriers (see Voit 1992; Smith et al. 2007; Veilleux et al. 2009a). It is still unclear whether the ionization state of grains is actually related to infrared luminosity (e.g., Desai et al. 2007; Smith et al. 2007; Veilleux et al. 2009a; Imanishi et al. 2010a; Petric et al. 2011).

### 5.2.2. Dust extinction as a function of infrared color

In Figure 11, we present the  $\text{Br}\alpha/\text{H}\beta$  line ratio of (U)LIRGs as a function of *IRAS* 25–60  $\mu\text{m}$  color. There is an anti-correlation between the two parameters with Spearman rank correlation coefficient =  $-0.67$  and the probability of obtaining the correlation by chance =  $0.02$ . This supports that warmer sources are less extinguished than cooler sources (see Veilleux et al. 1999a, 2009a; Keel et al. 2005; Imanishi et al. 2008). When using Balmer decrement values instead, such a correlation becomes weaker since the optical lines do not trace well the buried sources.

## 6. SUMMARY

We obtained *AKARI* 2.5–5  $\mu\text{m}$  spectra of 36 (U)LIRGs, selected mainly from the *IRAS*-detected galaxies in the SDSS. We measured the NIR spectral features including continuum slope, 3.3  $\mu\text{m}$  PAH strength, optical depths at 3.1 and 3.4  $\mu\text{m}$ , and Bracket lines in order to find AGN signatures. Together with samples in the literature and ancillary data, we compared optical and infrared properties of (U)LIRGs. Our primary results are summarized below.

1. We found that 52% (14/27) of optical non-Seyfert galaxies in our (U)LIRG sample show the AGN signature in their NIR spectra. The NIR AGN detection rate for the combined sample is higher in composite (U)LIRGs than in SF (U)LIRGs, and increases with infrared luminosity.
2. We fitted the *IRAS* photometric data for 69 (U)LIRGs with the AGN/starburst SED templates to compute the AGN contribution to the infrared luminosity. We found that the contribution of buried AGN to the infrared luminosity is 5–10%, smaller than the typical AGN contribution in (U)LIRGs including Seyfert galaxies (10–40%).

3. The NIR continuum slopes correlate well with *WISE* [3.4]–[4.6] colors. Using the *WISE* [3.4]–[4.6] color vs. *IRAS* 25–60  $\mu\text{m}$  color domain, we found sources associated with warm dust emission, but without hot dust emission. The *WISE* color is useful for identifying a large number of AGN, while it can miss heavily obscured AGN.

We are grateful to an anonymous referee for his/her comments that helped to improve the manuscript. This work was supported by Mid-career Research Program through NRF grant funded by the MEST (No.2010-0013875). J.C.L., M.K., and J.H.L. are members of the Dedicated Researchers for Extragalactic AstronoMy (DREAM) in Korea Astronomy and Space Science Institute (KASI). H.S.H. acknowledges the Centre National d’Etudes Spatiales (CNES) and the Smithsonian Institution for the support of his post-doctoral fellowship. This research is based on observations with *AKARI*, a JAXA project with the participation of ESA. Funding for the SDSS and SDSS-II has been provided by the Alfred P. Sloan Foundation, the Participating Institutions, the National Science Foundation, the U.S. Department of Energy, the National Aeronautics and Space Administration, the Japanese Monbukagakusho, the Max Planck Society, and the Higher Education Funding Council for England. The SDSS Web Site is <http://www.sdss.org/>. The SDSS is managed by the Astrophysical Research Consortium for the Participating Institutions. The Participating Institutions are the American Museum of Natural History, Astrophysical Institute Potsdam, University of Basel, University of Cambridge, Case Western Reserve University, University of Chicago, Drexel University, Fermilab, the Institute for Advanced Study, the Japan Participation Group, Johns Hopkins University, the Joint Institute for Nuclear Astrophysics, the Kavli Institute for Particle Astrophysics and Cosmology, the Korean Scientist Group, the Chinese Academy of Sciences (LAMOST), Los Alamos National Laboratory, the Max-Planck-Institute for Astronomy (MPIA), the Max-Planck-Institute for Astrophysics (MPA), New Mexico State University, Ohio State University, University of Pittsburgh, University of Portsmouth, Princeton University, the United States Naval Observatory, and the University of Washington. This publication makes use of data products from the *Wide-field Infrared Survey Explorer*, which is a joint project of the University of California, Los Angeles, and the Jet Propulsion Laboratory, California Institute of Technology, funded by the National Aeronautics and Space Administration.

## REFERENCES

- Abel, N. P., Dudley, C., Fischer, J., Satyapal, S., & van Hoof, P. A. M. 2009, *ApJ*, 701, 1147
- Abazajian, K. N., et al. 2009, *ApJS*, 182, 543

- Adelman-McCarthy, J. K., et al. 2006, *ApJS*, 162, 38
- Assef, R. J., et al. 2010, *ApJ*, 713, 970
- Baldwin, J. A., Phillips, M. M., & Terlevich, R. 1981, *PASP*, 93, 5
- Bauer, F. E., Yan, L., Sajina, A., Alexander, D. M. 2010, *ApJ*, 710, 212
- Boquien, M., et al. 2012, *A&A*, 539, 145
- Brinchmann, J., Charlot, S., White, S. D. M., Tremonti, C., Kauffmann, G., Heckman, T., & Brinkmann, J. 2004, *MNRAS*, 351, 1151
- Calzetti, D., Armus, L., Bohlin, R. C., Kinney, A. L., Koornneef, J., & Storchi-Bergmann, T. 2000, *ApJ*, 533, 682
- Cao, C., Wu, H., Wang, J. L., Hao, C. N., Deng, Z. G., Xia, X. Y., & Zou Z. L. 2006, *Chinese J. Astron. Astrophys.*, 6, 197
- Cardelli, J. A., Clayton, G. C., & Mathis, J. S. 1989, *ApJ*, 345, 245
- Colless, M., et al. 2001, *MNRAS*, 328, 1039
- Dasyra, K. M., et al. 2006, *ApJ*, 651, 835
- de Grijp, M. H. K., Miley, G. K., Lub, J., & de Jong, T. 1985, *Nature*, 314, 240
- De Propris, R., et al. 2004, *MNRAS*, 351, 125
- Desai, V., et al. 2007, *ApJ*, 669, 810
- Donoso, E., et al. 2012, *ApJ*, 748, 80
- Draine, B. T. 1989, in *ESLAB Symp. 22 Infrared Spectroscopy in Astronomy*, ed. B. H. Kaldich (ESASP-290; Paris: ESA), 93
- Draine, B. T. 2003, *ARA&A*, 41, 241
- Elbaz, D., et al. 2007, *A&A*, 468, 33
- Elbaz, D., et al. 2010, *A&A*, 518, L29
- Elbaz, D., Dickinson, M., Hwang, H. S., et al. 2011, *A&A*, 533, A119
- Farrah, D., Afonso, J., Efstathiou, A., Rowan-Robinson, M., Fox, M., & Clements, D. 2003, *MNRAS*, 343, 585

- Farrah, D., et al. 2007, *ApJ*, 667, 149
- Genzel, R., Tacconi, L. J., Rigopoulou, D., Lutz, D., & Tecza M., 2001, *ApJ*, 563, 527
- Goto, T. 2005, *MNRAS*, 360, 322
- Goto, T., et al. 2011, *MNRAS*, 410, 573
- Haan, S., et al. 2011, *AJ*, 141, 100
- Hatziminaoglou, E., et al. 2010, *A&A*, 518, L33
- Hopkins, A. M., et al. 2003, *ApJ*, 599, 971
- Hou, L. G., Wu, X., & Han, J. L. 2009, *ApJ*, 704, 789
- Hwang, H. S., Elbaz, D., Lee, J. C., Jeong, W.-S., Park, C., Lee, M. G., & Lee, H. M. 2010a, *A&A*, 522, 33
- Hwang, H. S., Serjeant, S., Lee, M. G., Lee, K. H., & White, G. J. 2007, *MNRAS*, 375, 115
- Hwang, H. S., et al. 2010b, *MNRAS*, 409, 75
- Ideue, Y., et al. 2009, *ApJ*, 700, 971
- Imanishi, M. 2002, *ApJ*, 569, 44
- Imanishi, M. 2009, *ApJ*, 694, 751
- Imanishi, M., & Dudley, C. C. 2000, *ApJ*, 545, 701
- Imanishi, M., Dudley, C. C., & Maloney, P. R. 2006, *ApJ*, 637, 114
- Imanishi, M., Ichikawa, K., Takeuchi, T., Kawakatu, N., Oi, N., & Imase, K. 2011, *PASJ*, 63, 447
- Imanishi, M., Nakagawa, T., Ohyama, Y., Shirahata, M., Wada, T., Onaka, T., & Oi, N. 2008, *PASJ*, 60, 489
- Imanishi, M., Nakagawa, T., Shirahata, M., Ohyama, Y., & Onaka, T. 2010a, *ApJ*, 721, 1233
- Imanishi, M., Nakanishi, K., Tamura, Y., & Peng, C.-H. 2009, *AJ*, 128, 2037
- Imanishi, M., Nakanishi, K., Yamada, M., Tamura, Y., & Kohno, K. 2010b, *PASJ*, 62, 201
- Imanishi, M., & Maloney, P. R. 2003, *ApJ*, 588, 165



- Jarrett, T. H., Chester, T., Cutri, R., Schneider, S., Skrutskie, M., & Huchra, J. P. 2000, *AJ*, 119, 2498
- Jarrett, T. H., et al. 2011, *ApJ*, 735, 112
- Jones, D. H., et al. 2004, *MNRAS*, 355, 747
- Jones, D. H., Saunders, W., Read, M., & Colless, M. 2005, *Publ. Astron. Soc. Australia*, 22, 277
- Kartaltepe, J. S., Sanders, D. B., Le Floch, E., et al. 2010, *ApJ*, 721, 98
- Kartaltepe, J. S., Dickinson, M., Alexander, D. M., et al. 2011, *ApJ*, submitted (arXiv:1110.4057)
- Kauffmann, G., et al. 2003a, *MNRAS*, 341, 33
- Kauffmann, G., et al. 2003b, *MNRAS*, 346, 1055
- Kaviraj, S. 2009, *MNRAS*, 394, 1167
- Kawara, K., Hirashita, H., Nozawa, T., Kozasa, T., Oyabu, S., Matsuoka, Y., Shimizu, T., Sameshima, H., & Ienaka, N. 2011, *MNRAS*, 412, 1070
- Keel, W. C., Irby, B. K., May, A., Miley, G. K., Golombek, D., de Grijp, M. H. K., & Gallimore, J. F. 2005, *ApJS*, 158, 139
- Kennicutt, R. C. 1998, *ARA&A*, 36, 189
- Kewley, L. J., Groves, B., Kauffmann, G., & Heckman, T. 2006, *MNRAS*, 372, 961
- Kewley, L. J., Heisler, C. A., Dopita, M. A., & Lumsden S. 2001, *ApJS*, 132, 37
- Kim, D. -C., & Sanders, D. B. 1998, *ApJS*, 119, 41
- Kim, D. -C., Veilleux, S., & Sanders, D. B. 2002, *ApJS*, 143, 277
- Kormendy, J., & Sanders, D. B. 1992, *ApJ*, 390, L53
- Le Floch, E., et al. 2005, *ApJ*, 632, 169
- Lee, J. C., Hwang, H. S., Lee, M. G., Kim, M., & Kim, S. C. 2011, *MNRAS*, 414, 702
- Lee, J. H., Hwang, H. S., Lee, M. G., Lee, J. C., & Matsuhara, H. 2010a, *ApJ*, 719, 1954
- Leech, K. J., Rowan-Robinson, M., Lawrence, A., & Hughes, J. D. 1994, *MNRAS*, 267, 253

- Lonsdale, C. J., Farrah, D., & Smith, H. E., 2006, *Ultraluminous Infrared Galaxies*, ed. J. W. Mason (Springer Verlag), 285
- Lotz, J. M., et al. 2008, *ApJ*, 672, 177
- Lutz, D., Spoon, H. W. W., Rigopoulou, D., Moorwood, A. F. M., & Genzel, R. 1998, *ApJ*, 505, L103
- Magnelli, B., Elbaz, D., Chary, R. R., Dickinson, M., Le Borgne, D., Frayer, D. T., & Willmer, C. N. A. 2009, *A&A*, 496, 57
- Moorwood, A. F. M. 1986, *A&A*, 166, 4
- Moshir M., et al., 1992, Explanatory Supplement to the *IRAS* Faint Source Survey, Version 2, JPL D-10015 8/92. JPL, Pasadena
- Mouri, H., Kawara, K., Taniguchi, Y., & Nishida, M. 1990, *ApJ*, 356, L39
- Mullaney, J. R., Alexander, D. M., Goulding, A. D., & Hickox, R. C. 2011, 414, 1082
- Murakami, H., et al. 2007, *PASJ*, 59, 369
- Murphy, T. W., Soifer, B. T., Matthews, K., Armus, L., & Kiger, J. R. 2001, *AJ*, 121, 97
- Murphy, T. W., Soifer, B. T., Matthews, K., Kiger, J. R., & Armus, L. 1999, *ApJ*, 525, L85
- Nardini, E., Risaliti, G., Watabe, Y., Salvati, M., & Sani, E. 2010, *MNRAS*, 405, 2505
- Neff, S. G. & Hutchings, J. B. 1992, *AJ*, 103, 1746
- Neugebauer, G., et al. 1984, *ApJ*, 278, L1
- Nishiyama, S., Tamura, M., Hatano, H., Kato, D., Tanabe, T., Sugitani, K., & Nagata, T. 2009, *ApJ*, 696, 1407
- Ohya, Y., et al. 2007, *PASJ*, 59, 411
- Onaka, T., et al. 2007, *PASJ*, 59, 401
- Osterbrock, D. E., & Ferland, G. J. 2006, *Astrophysics of Gaseous Nebulae and Active Galactic Nuclei*, 2nd edn. University Science Books, Mill Valley, CA
- Petric, A. O., et al. 2011, *ApJ*, 730, 28
- Pozzi, F., et al. 2012, *MNRAS*, in press (arXiv:1204.1152)

- Rigopoulou, D., Spoon, H. W. W., Genzel, R., Lutz, D., Moorwood, A. F. M., & Tran, Q. D. 1999, *AJ*, 118, 2625
- Risaliti, G., Maiolino, R., Marconi, A., Sani, E., Berta, S., Braito, V., Della Ceca, R., Franceschini, A., & Salvati, M. 2006, *MNRAS*, 365, 303
- Risaliti, G., Imanishi, M., & Sani, E. 2010, *MNRAS*, 401, 197
- Rothberg, B., & Fischer, J. 2010, *ApJ*, 712, 318
- Sajina, A., Yan, L., Lutz, D., Steffen, A., Helou, G., Heynh, M., Frayer, D., Choi, P., Tacconi, L., & Dasyra, K. 2008, *ApJ*, 683, 659
- Sanders, D. B., Egami, E., Lipari, S., Mirabel, I. F., & Soifer, B. T. 1995, *AJ*, 110, 1993
- Sanders, D. B., Mazzarella, J. M., Kim, D.-C., Surace, J. A., & Soifer, B. T. 2003, *AJ*, 126, 1607
- Sanders, D. B., & Mirabel, I. F. 1996, *ARA&A*, 34, 749
- Sanders, D. B., Soifer, B. T., Elias, J. H., Madore, B. F., Matthews, K., Neugebauer, G., & Scoville, N. Z. 1988a, *ApJ*, 325, 74
- Sanders, D. B., Soifer, B. T., Elias, J. H., Neugebauer, G., & Matthews, K. 1988b, *ApJ*, 328, 35
- Sani, E., Risaliti, G., Salvati, M., Maiolino, ., Marconi, A., Berta, S., Braito, V., Della Ceca, R., & Franceschini, A. 2008, *ApJ*, 675, 96
- Shimizu, T., Kawara, K., sameshima, H., Ienaka, N., Nozawa, T., & Kozasa, T. 2011, *MNRAS*, 418, 625
- Smith, J. D., et al. 2007, *ApJ*, 656, 770
- Soifer, B. T., Boehmer, L., Neugebauer, G., & Sanders, D. B. 1989, *AJ*, 98, 766
- Soifer, B. T., Helou, G., & Werner, M. 2008, *ARA&A*, 46, 201
- Soifer, B. T., Sanders, D. B., Madore, B. F., Neugebauer, G., Danielson, G. E., Elias, J. H., Lonsdale, C. J., & Rice, W. L. 1987, *ApJ*, 320, 238
- Spoon, H. W. W., Marshall, J. A., Houck, J. R., Elitzur, M., Hao, L., Armus, L., Brandl, B. R., & Charmandaris, V. 2007, *ApJ*, 654, L49
- Stanford, S. A., Stern, D., van Breugel, W., & De Breuck, C. 2000, *ApJS*, 131, 185

- Stern, D., et al. 2012, ApJ, in press (arXiv:1205.0811)
- Tacconi, L. J., Genzel, R., Lutz, D., Rigopoulou, D., Baker, A. J., Iserlohe, C., & Tecza, M. 2002, ApJ, 580, 73
- Teng, S. H., & Veilleux, S. 2010, ApJ, 725, 1848
- Tokunaga, A. T., Sellgren, K., Smith, R. G., Nagata, T., Sakata, A., & Nakada, Y. 1991, ApJ, 380, 452
- Tran, Q. D., et al. 2001, ApJ, 552, 527
- Tremonti, C. A., et al. 2004, ApJ, 613, 898
- Valiante, E., Lutz, D., Sturm, E., Genzel, R., & Chapin, E. L. 2009, ApJ, 701, 1814
- Veilleux, S., Kim, D.-C., & Sanders, D. B. 1999, ApJ, 522, 113
- Veilleux, S., Kim, D.-C., & Sanders, D. B. 2002, ApJS, 143, 315
- Veilleux, S., Kim, D.-C., Sanders, D. B., Mazzarella, J. M., & Soifer, B. T. 1995, ApJS, 98, 171
- Veilleux, S., & Osterbrock, D. E. 1987, ApJS, 63, 295
- Veilleux, S., Sanders, D. B., & Kim, D.-C. 1997, ApJ, 484, 92
- Veilleux, S., Sanders, D. B., & Kim, D.-C. 1999, ApJ, 522, 139
- Veilleux, S., et al. 2009a, ApJS, 182, 628
- Veilleux, S., et al. 2009b, ApJ, 701, 587
- Véron-Cetty, M. -P, & Véron, P. 2006, A&A, 455, 773
- Voit, G. M. 1992, MNRAS, 258, 841
- Wang, J. L., Xia, X. Y., Mao, S., Cao, C., Wu, H., Deng, Z. G. 2006, ApJ, 649, 722
- Wright, E. L., et al. 2010, AJ, 140, 1868
- York, D. G., et al. 2000, AJ, 120, 1579
- Yuan, T.-T., Kewley, L. J., & Sanders, D. B. 2010, ApJ, 709, 884

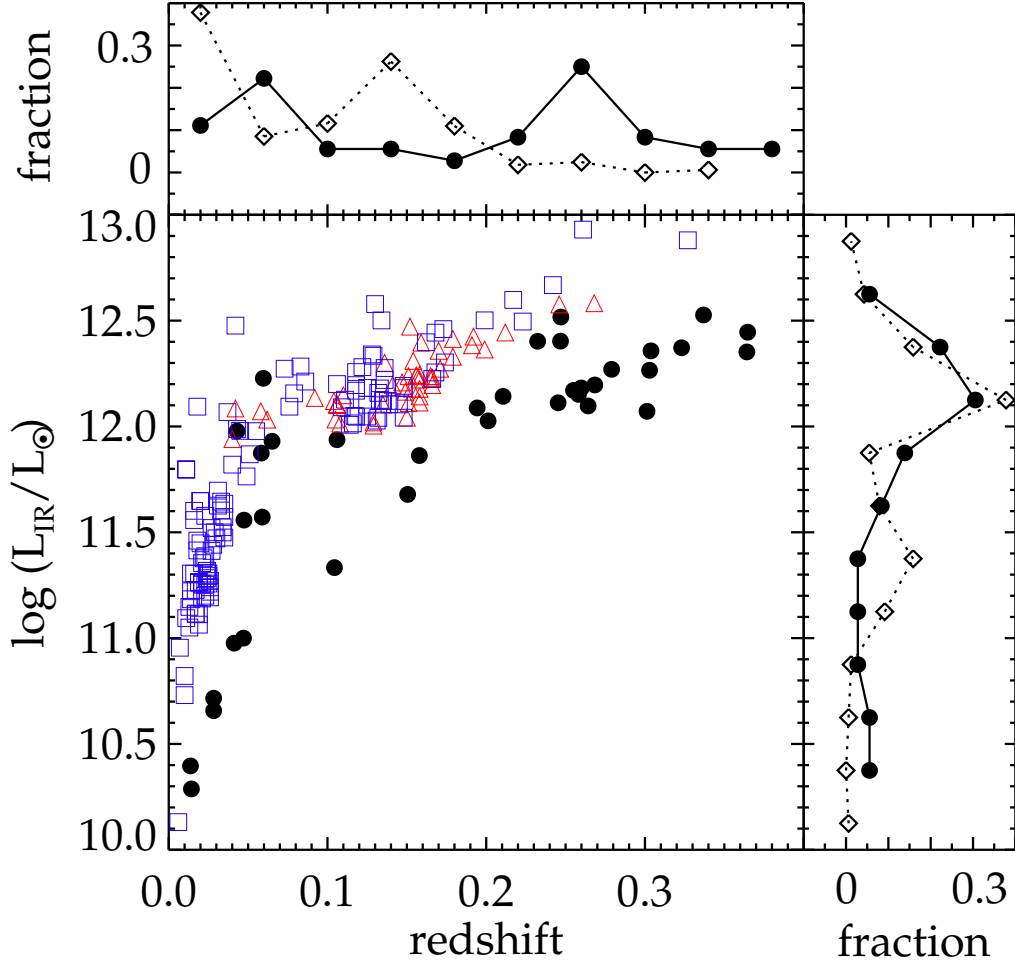


Fig. 1.— Infrared luminosity vs. redshift distribution of (U)LIRGs observed with *AKARI* IRC. The (U)LIRGs in this study, Imanishi et al. (2008), and Imanishi et al. (2010a) are represented by black filled circles, red open triangles, and blue open squares, respectively. In the upper and right panels, the redshift and luminosity distributions of (U)LIRGs are shown, respectively (our sample: solid line with filled circles; Imanishi sample: dotted line with open diamonds).

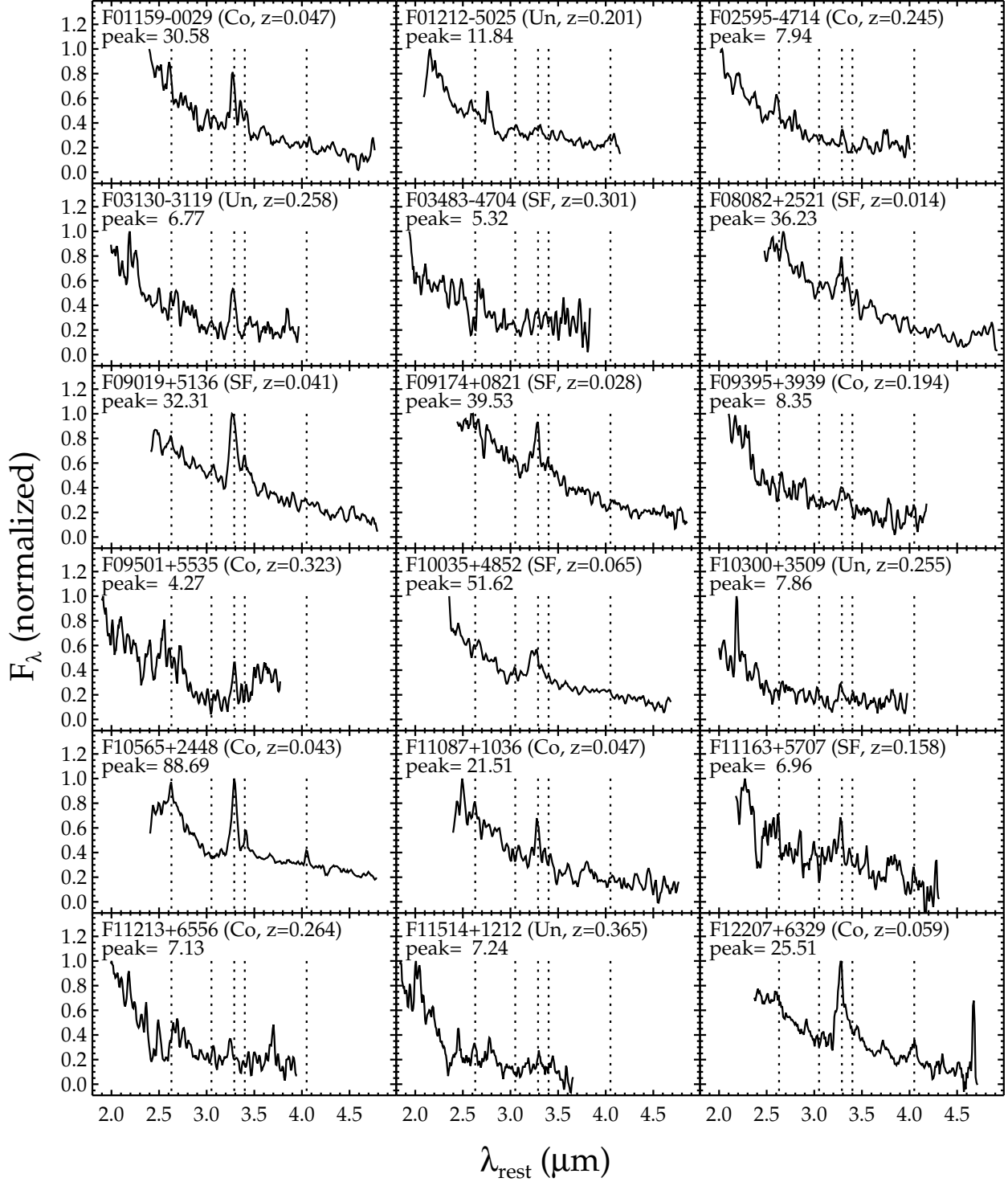


Fig. 2.— *AKARI* NIR spectra of 36 (U)LIRGs in our sample. For each object, their optical spectral type (SF=star-forming; Co=composite; LI=LINER; S2=Seyfert 2; S1=Seyfert 1; Un=Unclassified) and redshift are shown. The spectra presented here are smoothed using a 3 pixel box ( $\sim 0.03 \mu\text{m}$ ) and are normalized to peak values, denoted in units of  $10^{-13} \text{ ergs s}^{-1} \text{ cm}^{-2} \mu\text{m}^{-1}$ . The dotted lines indicate the wavelengths of Br $\beta$  (2.63  $\mu\text{m}$ ), H<sub>2</sub>O ice-covered dust absorption (3.05  $\mu\text{m}$ ), PAH emission (3.29  $\mu\text{m}$ ), bare carbonaceous dust absorption (3.4  $\mu\text{m}$ ), and Br $\alpha$  (4.05  $\mu\text{m}$ ) features.

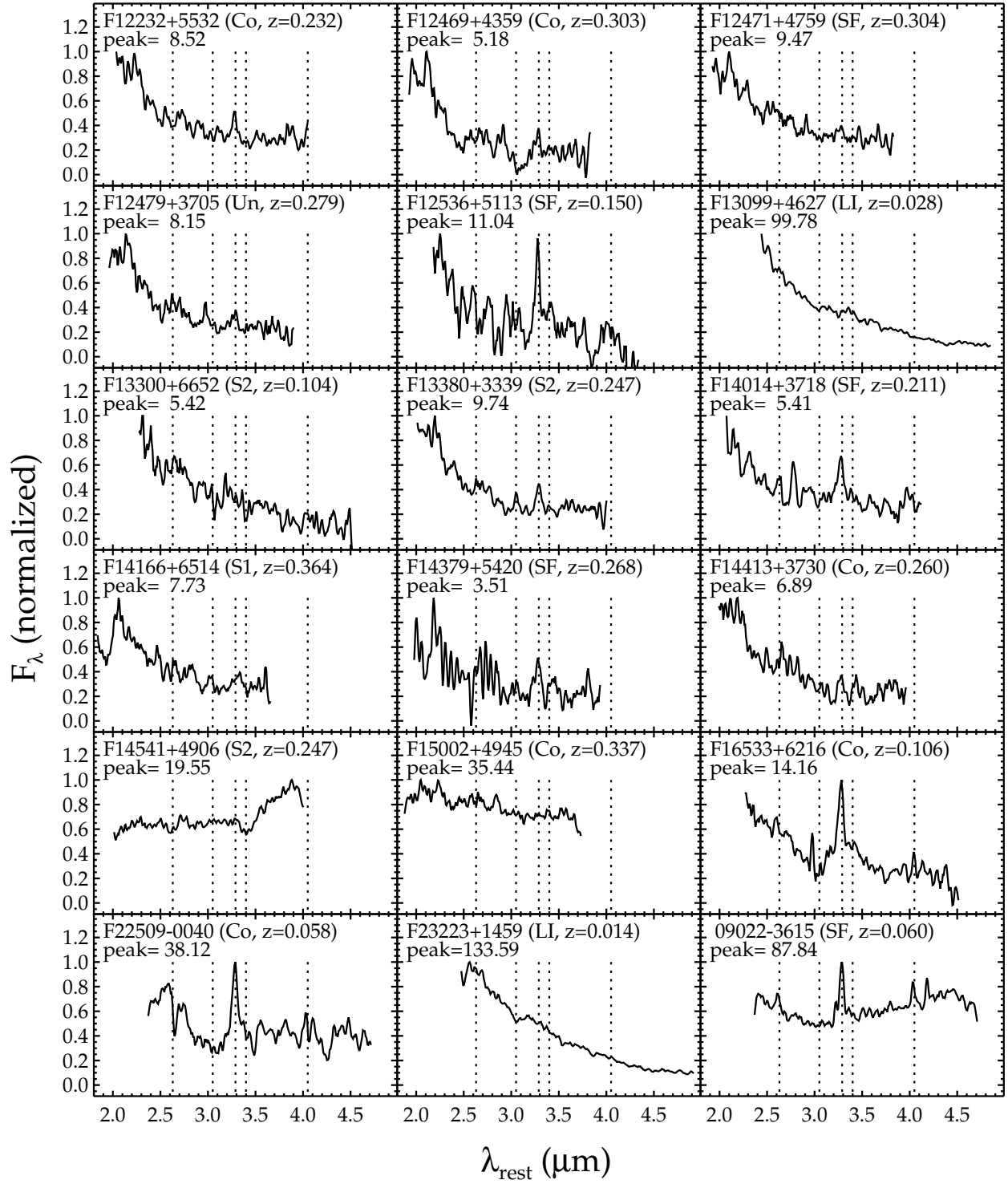


Fig. 2.— Continued

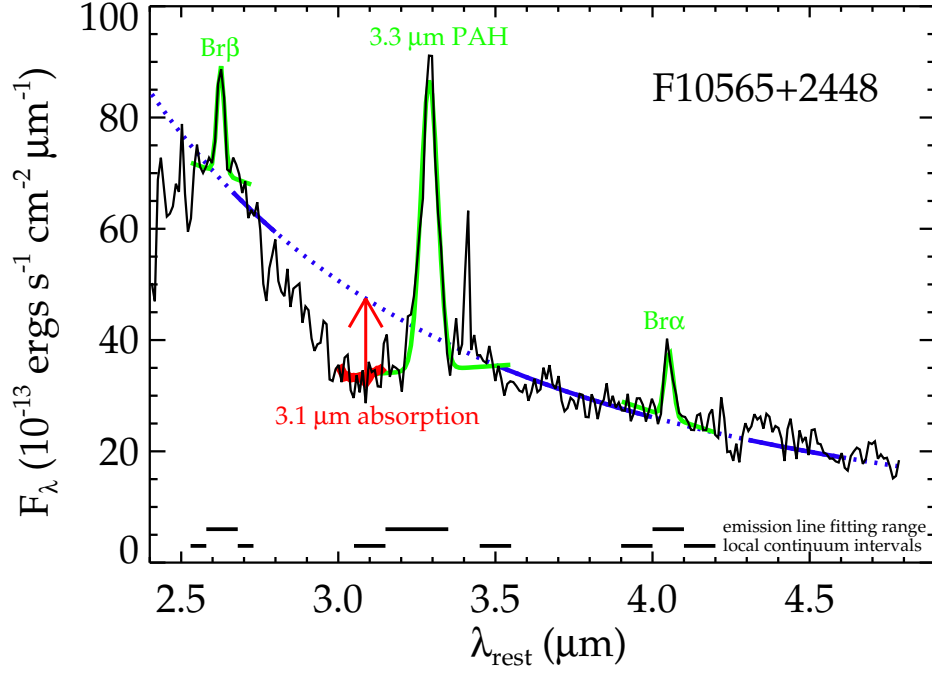


Fig. 3.— Example of spectral fitting for F10565+2448. The background solid line is the observed spectrum. The Gaussian fit lines to measure 2.63  $\mu\text{m}$  Br $\beta$ , 3.3  $\mu\text{m}$  PAH, and 4.05  $\mu\text{m}$  Br $\alpha$  emissions are overplotted. The solid-dotted power-law line represents the global continuum. The wavelength intervals not used in the continuum fit are denoted by dotted lines. The thick line around 3.1  $\mu\text{m}$  is the 10 pixel smoothed profile of 3.1  $\mu\text{m}$  absorption. The arrow shows the wavelength where the difference between the continuum level and absorption profile is maximized. In this case, 3.4  $\mu\text{m}$  absorption is not detected.



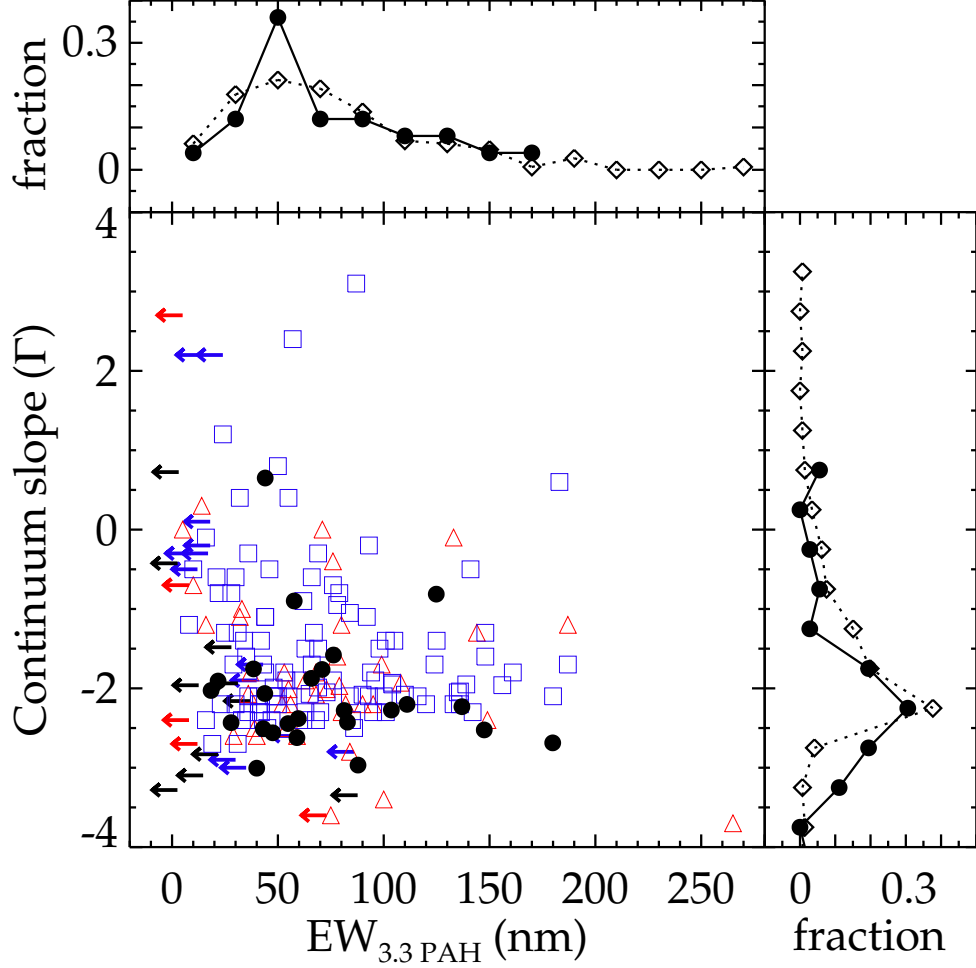


Fig. 4.—  $EW_{3.3PAH}$  vs. continuum slope  $\Gamma$  diagram. The (U)LIRGs in this study, Imanishi et al. (2008), and Imanishi et al. (2010a) are represented by black filled circles, red open triangles, and blue open squares, respectively. The sources with the upper limits of  $EW_{3.3PAH}$  are represented by arrows. The continuum slope  $\Gamma$  was defined by  $F_\lambda \propto \lambda^\Gamma$  in this study, while it was defined by  $F_\nu \propto \lambda^\Gamma$  in Imanishi et al. Thus,  $\Gamma_{\text{this study}}$  equals  $\Gamma_{\text{Imanishi}} - 2$ , and the values of  $\Gamma_{\text{this study}}$  and  $\Gamma_{\text{Imanishi}} - 2$  are presented for fair comparison. The  $EW_{3.3PAH}$  and continuum slope distributions are shown in the upper and right panels, respectively (our sample: solid line with filled circles; Imanishi sample: dotted line with open diamonds). In the upper panel, the (U)LIRGs with  $EW_{3.3PAH}$  upper limits are not included.

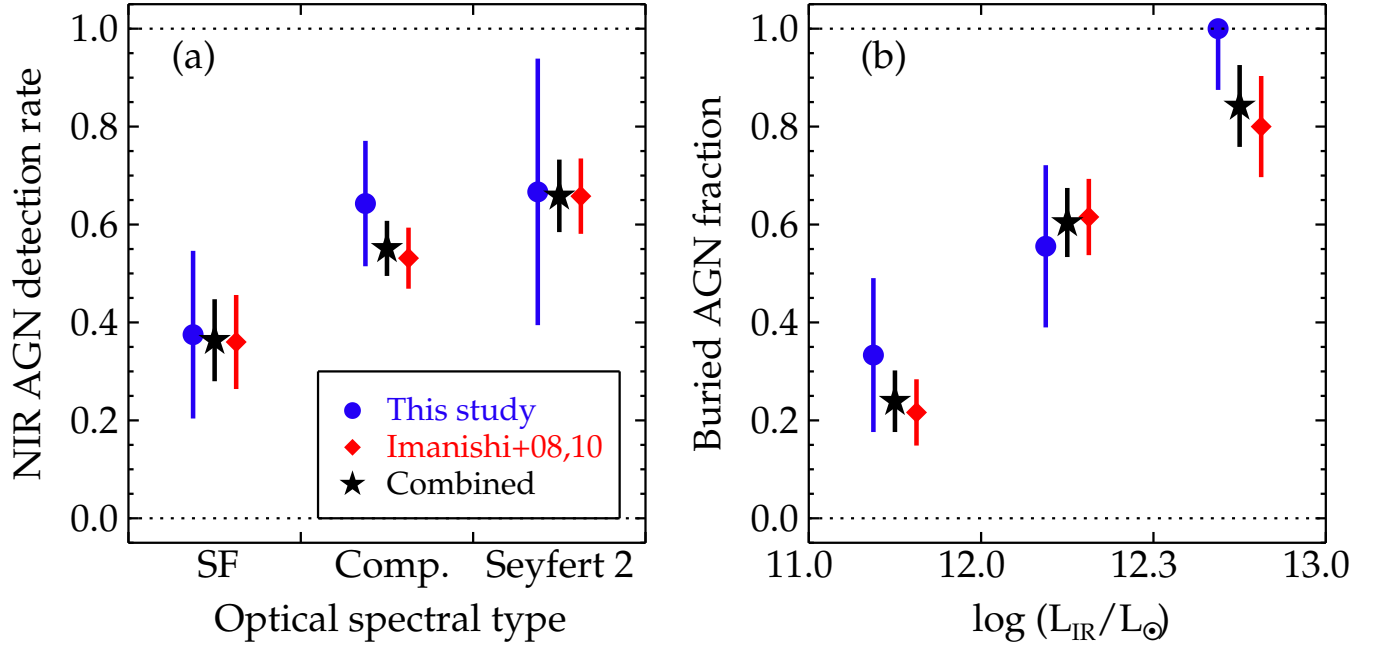


Fig. 5.— (a) *AKARI*-based AGN detection rate as a function of optical spectral type (See Section 5.1.1 for the definition of AGN signatures in the NIR spectra). (b) Buried AGN fraction as a function of infrared luminosity. The buried AGN fraction means the number fraction of NIR AGN among optical non-Seyfert galaxies. The blue circles, red diamonds, and black stars indicate the results from our sample, Imanishi sample, and the combined sample, respectively. The error bars are based on Poisson statistics (see De Propriis et al. 2004).

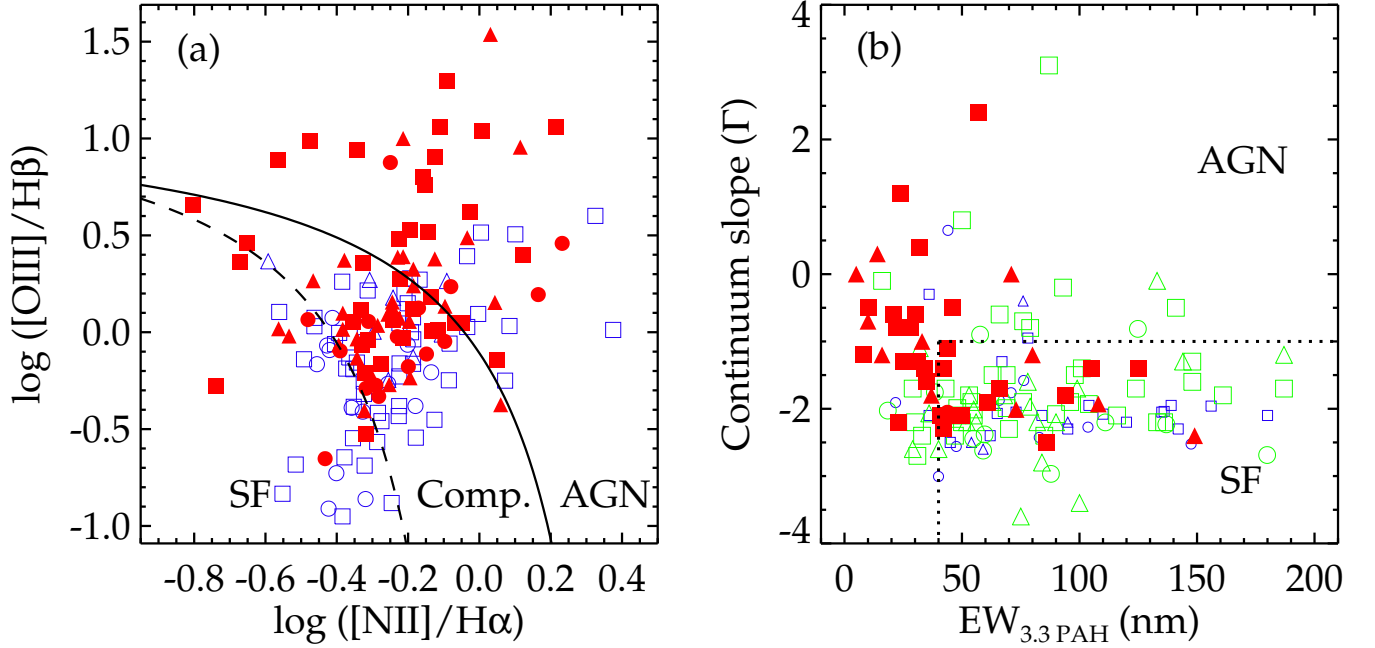


Fig. 6.— (a) Optical diagnostic diagram based on  $[\text{OIII}]\lambda 5007/\text{H}\beta$  and  $[\text{NII}]\lambda 6584/\text{H}\alpha$  line ratios. The (U)LIRGs in this study, Imanishi et al. (2008), and Imanishi et al. (2010a) are represented by circles, triangles, and squares, respectively. The optical line ratios of the Imanishi sample are taken from Veilleux et al. (1995, 1999a) and Kewley et al. (2001). The sources with (/without) AGN signatures in their NIR spectra are denoted by red filled (/blue open) symbols. The solid and dashed lines indicate the maximum starburst (Kewley et al. 2001) and pure star formation (Kauffmann et al. 2003b) lines, respectively. (b) NIR diagnostic diagram based on  $\text{EW}_{3.3\text{PAH}}$  and continuum slope  $\Gamma$ . The optical SF, composite, and AGN (LINER + Seyfert) sources are denoted by small blue open, large green open, and large red filled symbols, respectively. The (U)LIRGs optically unclassified or with upper limits are not included. The dotted line shows the AGN selection criteria in this study:  $\text{EW}_{3.3\text{PAH}} < 40$  nm or  $\Gamma > -1$ .

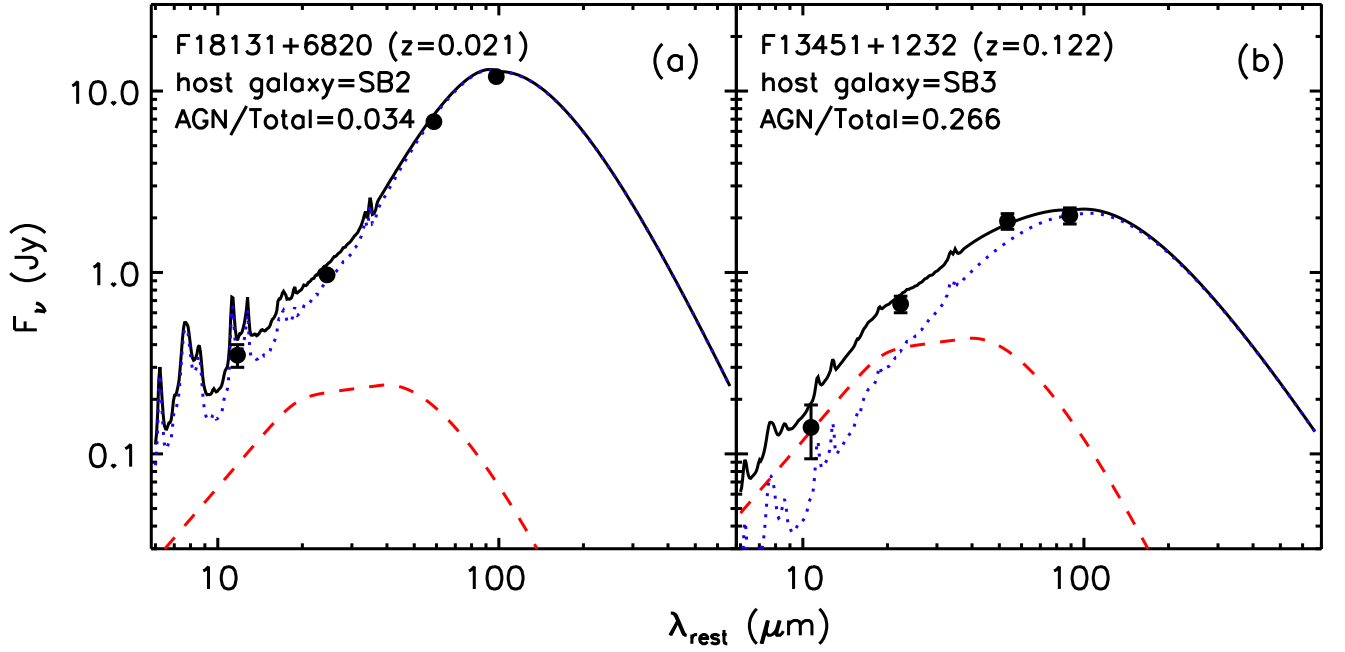


Fig. 7.— The best fit SEDs for (a) F18131+6820 and (b) F13451+1232 derived using the infrared SED-fitting routine, DECOMPIR (Mullaney et al. 2011). The filled circles with errorbars indicate their four *IRAS* flux densities. The black solid, blue dotted, and red dashed lines represent the total, host-galaxy, and AGN SEDs, respectively. The labels in the upper left indicate which host-galaxy template is used and the derived AGN contribution to the total infrared luminosity.

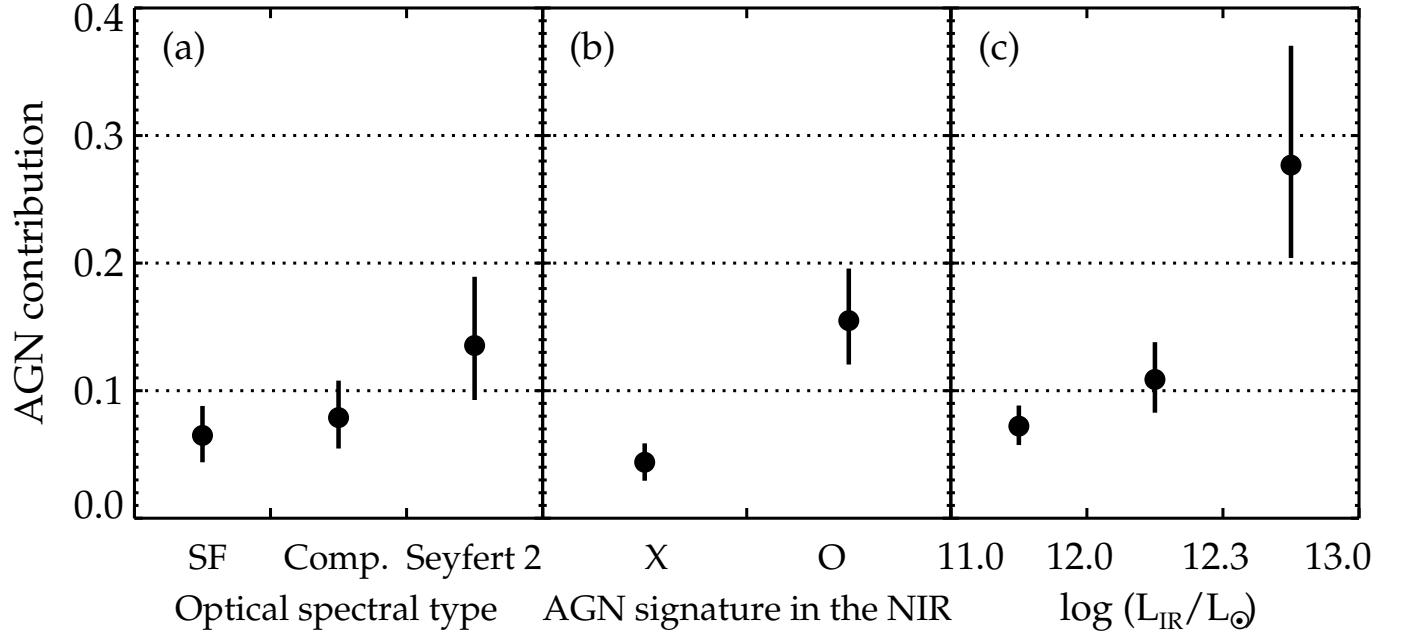


Fig. 8.— The AGN contribution to the infrared luminosities of (U)LIRGs in bins of (a) optical spectral type, (b) presence of AGN signature in the NIR spectra, and (c) infrared luminosity. The mean values with sampling errors are shown.

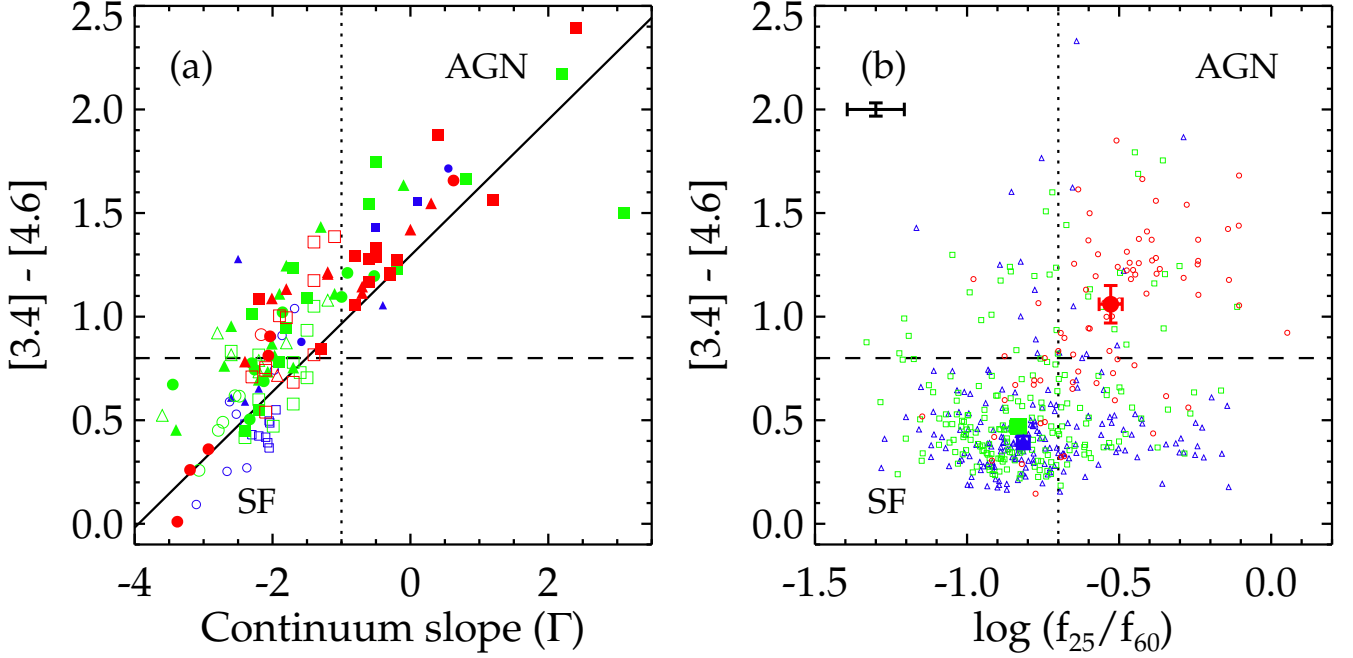


Fig. 9.— (a) Comparison between the *WISE*  $[3.4]$ – $[4.6]$  color (Vega) and NIR continuum slope  $\Gamma$  for (U)LIRGS observed with *AKARI* IRC. The (U)LIRGS in this study, Imanishi et al. (2008), and Imanishi et al. (2010a) are represented by circles, triangles, and squares, respectively. The optical composite and AGN (/SF) sources are denoted by large (/small) symbols, and the sources with (/without) AGN signature in NIR spectra are shown by filled (/open) symbols. The symbols are also color-coded according to optical spectral types (blue: SF; green: composite; red: AGN). The solid line represents the *WISE* colors expected from simple power-law continuum models ( $F_\lambda \propto \lambda^\Gamma$ ). The vertical dotted and horizontal dashed lines indicate the criteria separating AGN from SF-dominated galaxies in this study and Stern et al. (2012), respectively. (b) The *WISE*  $[3.4]$ – $[4.6]$  color vs. *IRAS* flux density ratio of 25 to 60  $\mu\text{m}$  diagram. The small open symbols are (U)LIRGs in SDSS DR7 (Hwang et al. 2010a). Their median values are denoted by large filled symbols with sampling errors. The red circles, green squares, and blue triangles are for AGN, composite and SF galaxies determined in the optical spectra. The (U)LIRGs with S/Ns  $> 3$  at (*WISE*) 3.4, 4.6, (*IRAS*) 25, 60  $\mu\text{m}$  are only presented. The error bars in the upper-left corner indicate the typical uncertainties associated with the colors. The vertical dotted and horizontal dashed lines indicate the criteria separating AGN from SF-dominated galaxies in Sanders et al. (1988b) and Stern et al. (2012), respectively.

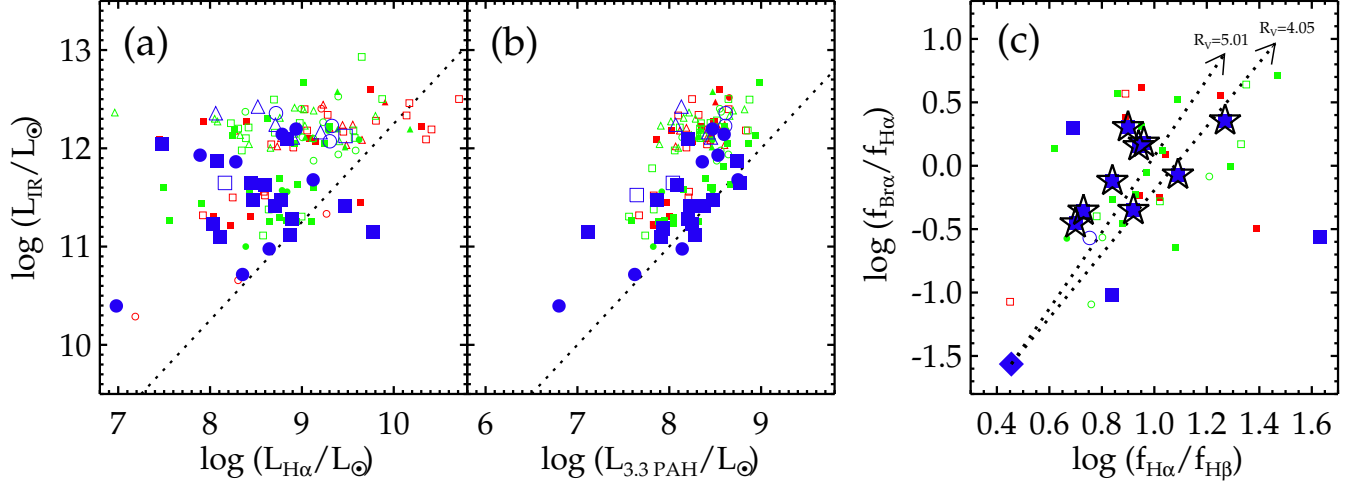


Fig. 10.— Comparisons of infrared luminosity with (a)  $\text{H}\alpha$  and (b)  $3.3\text{ }\mu\text{m}$  PAH luminosities. The (U)LIRGs in this study, Imanishi et al. (2008), and Imanishi et al. (2010a) are represented by circles, triangles, and squares, respectively. The optical SF (/composite and AGN) sources are denoted by large (/small) symbols, and the sources without (/with) AGN signature in NIR spectra are shown by filled (/open) symbols. The symbols are also color-coded according to optical spectral types (blue: SF; green: composite; red: AGN). In each panel, the dotted line indicates the SF galaxy sequence (see Section 5.2.1). (c) Comparison between the observed  $\text{Br}\alpha/\text{H}\alpha$  and  $\text{H}\alpha/\text{H}\beta$  line ratios. The symbols are the same as in panels (a–b), but the diamond in the lower-left corner indicates the intrinsic position of SF galaxies in this plane (case B theory; Osterbrock & Ferland 2006). The reddening vectors of  $A_V = 8$  mag from the Calzetti et al. (2000) extinction curve with  $R_V = 4.05$  and  $5.01$  are shown by dotted line arrows. Since the curve is given at shorter wavelengths than  $2.2\text{ }\mu\text{m}$ , the extinction at  $4.05\text{ }\mu\text{m}$  ( $A_{\text{Br}\alpha}$ ) is extrapolated from  $A_{2.2\text{ }\mu\text{m}}$  using the model of  $A_{\lambda} \propto \lambda^{-1.75}$  (e.g., Cardelli et al. 1989; Draine 1989; but see also Nishiyama et al. 2009). We fit a linear relation to the data of pure SF (U)LIRGs after removing three outliers with  $2\sigma$  clipping (open star symbols), and so obtain the curve with  $R_V = 5.01$ .

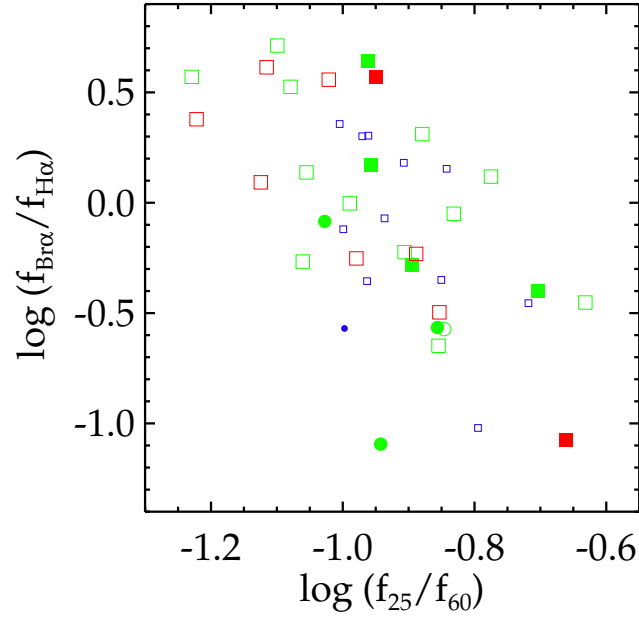


Fig. 11.— The Br $\alpha$ /H $\alpha$  line ratio vs. *IRAS* flux density ratio between 25 and 60  $\mu$ m for the *AKARI* (U)LIRG sample. The symbols are the same as in Figure 9 (a).



Table 1. Basic information and optical spectral properties.

Object (1)	RA (2)	Dec (3)	z (4)	$f_{12}$ (5)	$f_{25}$ (6)	$f_{60}$ (7)	$f_{100}$ (8)	$\log L_{\text{IR}}$ (9)	Type (10)	H $\alpha$ /H $\beta$ (11)	$\log L_{\text{H}\alpha}$ (12)	[OIII]/H $\beta$ (13)	[NII]/H $\alpha$ (14)	Ref. (15)
F01159–0029	01 18 34.1	–00 13 42	0.047	<0.222	0.335	3.476	5.013	11.56	Co	6.94	8.78	0.42	0.66	1/2
F01212–5025	01 23 19.9	–50 09 30	0.201	<0.056	<0.077	0.415	0.717	12.03	Un	...	...	...	...	3
F02595–4714	03 01 17.6	–47 02 14	0.245	<0.090	<0.063	0.268	0.484	12.11	Co	5.69	8.94	1.33	0.68	3/4
F03130–3119	03 15 03.5	–31 07 48	0.258	<0.087	<0.103	0.252	0.438	12.15	Un	...	...	...	...	3
F03483–4704	03 49 55.3	–46 55 20	0.301	<0.083	<0.098	0.156	<0.542	12.07	SF	4.78	9.24	0.80	0.41	3/4
F08082+2521	08 11 13.5	+25 12 24	0.014	0.124	0.251	2.243	6.116	10.40	SF	5.39	6.92	0.12	0.38	1/2
F09019+5136	09 05 28.9	+51 24 49	0.041	0.096	0.113	0.946	1.683	10.98	SF	5.27	8.58	0.19	0.40	1/2
F09174+0821	09 20 08.6	+08 09 01	0.028	<0.102	0.155	1.339	2.212	10.72	SF	5.46	8.29	0.14	0.48	1/2
F09395+3939	09 42 39.2	+39 26 00	0.194	<0.067	<0.102	0.470	1.014	12.09	Co	8.17	9.56	0.54	0.55	1/2
F09501+5535	09 53 31.9	+55 21 02	0.323	<0.076	<0.101	0.352	<0.831	12.37	Co	4.17	8.32	0.77	0.71	1/2
F10035+4852	10 06 45.9	+48 37 44	0.065	0.098	0.283	4.593	6.242	11.93	SF	6.68	7.83	0.39	0.47	1/2
F10300+3509	10 32 53.9	+34 53 59	0.255	<0.110	<0.091	0.192	0.639	12.17	Un	...	...	...	...	5
F10565+2448	10 59 18.1	+24 32 34	0.043	0.217	1.138	12.120	15.130	11.98	Co	16.20	9.52	0.51	0.48	6/7,8
F11087+1036	11 11 18.7	+10 20 20	0.047	<0.188	<0.164	0.745	1.248	11.00	Co	5.56	8.33	0.86	0.63	1/2
F11163+5707	11 19 11.2	+56 50 52	0.158	<0.071	<0.076	0.525	0.743	11.86	SF	3.82	8.22	0.68	0.35	1/2
F11213+6556	11 24 24.6	+65 39 46	0.264	<0.094	<0.124	0.240	<0.908	12.10	Co	7.04	9.07	0.90	0.80	1/2
F11514+1212	11 54 02.7	+11 55 28	0.365	<0.123	<0.131	0.236	<0.967	12.45	Un	...	...	...	...	3
F12207+6329	12 23 05.3	+63 13 21	0.059	<0.125	0.308	2.160	3.310	11.57	Co	4.64	8.73	1.19	0.39	1/2
F12232+5532	12 25 38.3	+55 15 49	0.232	<0.241	<0.095	0.601	0.941	12.40	Co	6.21	8.93	1.14	0.49	1/2
F12469+4359	12 49 16.6	+43 42 55	0.303	<0.109	<0.127	0.274	<0.656	12.27	Co	5.62	9.17	0.53	0.51	1/2
F12471+4759	12 49 27.9	+47 42 50	0.304	<0.118	<0.067	0.357	<1.168	12.36	SF	4.47	8.66	0.22	0.37	1/2
F12479+3705	12 50 18.2	+36 49 14	0.279	<0.109	<0.130	0.250	0.480	12.27	Un	...	...	...	...	5
F12536+5113	12 55 48.4	+50 57 17	0.150	<0.081	<0.100	0.398	<1.097	11.68	SF	5.08	9.06	0.41	0.44	1/2
F13099+4627	13 12 06.3	+46 11 46	0.028	<0.121	<0.150	0.998	2.556	10.66	LI	4.44	8.25	1.72	0.83	1/2
F13300+6652	13 31 40.0	+66 36 34	0.104	<0.088	<0.075	0.424	<0.795	11.33	S2	15.80	9.21	2.88	1.71	1/2
F13380+3339	13 40 14.4	+33 24 45	0.247	<0.108	<0.136	0.939	1.098	12.51	S2	...	...	...	...	9/10
F14014+3718	14 03 37.8	+37 03 55	0.211	<0.143	<0.136	0.381	0.707	12.14	SF	4.83	8.73	0.85	0.37	1/2
F14166+6514	14 17 53.7	+65 00 25	0.364	<0.069	<0.056	0.189	<1.488	12.35	S1	...	...	...	...	11/11
F14379+5420	14 39 30.6	+54 08 07	0.268	<0.064	<0.053	0.333	0.428	12.20	SF	5.19	8.88	0.81	0.38	1/2
F14413+3730	14 43 19.6	+37 18 01	0.260	<0.063	<0.068	0.311	0.533	12.18	Co	6.06	9.23	0.62	0.73	1/2
F14541+4906	14 55 49.4	+48 54 36	0.247	<0.082	0.200	0.530	0.543	12.40	LI	4.05	9.15	7.51	0.56	1/2
F15002+4945	15 01 50.5	+49 33 38	0.337	<0.053	0.074	0.395	0.510	12.53	Co	5.12	9.34	0.95	0.59	1/2
F16533+6216	16 53 52.1	+62 11 50	0.106	<0.059	0.169	1.480	2.503	11.94	Co	5.75	9.34	0.47	0.52	1/2
F22509–0040	22 53 33.0	–00 24 43	0.058	<0.174	0.716	5.143	5.028	11.87	Co	6.34	9.07	0.66	0.63	1/2

Table 1—Continued

Object (1)	RA (2)	Dec (3)	z (4)	$f_{12}$ (5)	$f_{25}$ (6)	$f_{60}$ (7)	$f_{100}$ (8)	$\log L_{\text{IR}}$ (9)	Type (10)	$\text{H}\alpha/\text{H}\beta$ (11)	$\log L_{\text{H}\alpha}$ (12)	$[\text{OIII}]/\text{H}\beta$ (13)	$[\text{NII}]/\text{H}\alpha$ (14)	Ref. (15)
F23223+1459	23 24 49.4	+15 16 32	0.014	0.144	<0.339	1.310	4.461	10.29	LI	3.89	7.13	1.56	1.46	1/2
09022−3615	09 04 12.7	−36 27 01	0.060	0.211	1.154	11.470	11.430	12.22	SF	5.67	9.27	1.16	0.33	12/4

Note. — Column 1: Object name in the *IRAS* catalogs. Columns 2–3: Right ascension and declination in units of  $^{\text{h}}\text{ }^{\text{m}}\text{ }^{\text{s}}$  and  $^{\circ}\text{ }'\text{ }''$ , respectively (J2000). Column 4: Redshift. Columns 5–8: The *IRAS* flux densities at 12, 25, 60, and 100  $\mu\text{m}$  (Jy). Column 9: Logarithm of infrared luminosity ( $L_{\odot}$ ), derived from the *IRAS* fluxes using the formula,  $L_{\text{IR}} = 2.1 \times 10^{39} \times D(\text{Mpc})^2 \times (13.48 \times f_{12} + 5.16 \times f_{25} + 2.58 \times f_{60} + f_{100})$ , in Sanders & Mirabel (1996). For sources with upper limits, we follow the method described in Imanishi et al. (2008, 2010a). The upper and lower limits on the infrared luminosity are obtained by assuming that the actual flux is equal to the *IRAS* upper limit and zero value, respectively, and the average of these values is adopted as the infrared luminosity. Column 10: Optical spectral type, determined with spectroscopic data covering at least from  $\text{H}\beta + [\text{OIII}]\lambda 5007$  to  $\text{H}\alpha + [\text{NII}]\lambda 6584$  using the criteria of Kewley et al. (2006) (SF=star-forming; Co=composite; LI=LINER; S2=Seyfert 2; S1=Seyfert 1; Un=Unclassified). Column 11: Observed  $\text{H}\alpha/\text{H}\beta$  ratio. Column 12: Logarithm of  $\text{H}\alpha$  luminosity ( $L_{\odot}$ ), corrected for dust extinction using the observed  $\text{H}\alpha/\text{H}\beta$  ratio with the Calzetti et al. (2000) extinction law ( $R_V = 4.05$ ) on assuming the intrinsic  $\text{H}\alpha/\text{H}\beta$  ratio of 2.85 for SF galaxies and 3.1 for composite plus AGN galaxies (Osterbrock & Ferland 2006). For SDSS (U)LIRGs in Hwang et al. (2010a), the aperture correction is also applied following the method suggested by Hopkins et al. (2003) based on the difference between fiber and Petrosian magnitudes to minimize the small fixed-size ( $3''$ ) aperture effect, if available. Column 13:  $[\text{OIII}]\lambda 5007/\text{H}\beta$  ratio, corrected for dust extinction. Column 14:  $[\text{NII}]\lambda 6584/\text{H}\alpha$  ratio, corrected for dust extinction. Column 15: References of the identification/optical properties. (1) Hwang et al. 2010a; (2) This study; (3) Hwang et al. 2007; (4) Lee et al. 2011; (5) Stanford et al. 2000; (6) Soifer et al. 1989; (7) Veilleux et al. 1995; (8) Yuan et al. 2010; (9) Leech et al. 1994; (10) Véron-Cetty & Véron 2006; (11) Hou et al. 2009; (12) Sanders et al. 2003.

Table 2. Observation log.

Object	Program	Observation ID	Observation Date
F01159–0029	CLNSL	3350035-001-002 <sup>a</sup>	2009-07-09
F01212–5025	NULIZ	3050012-001-002	2006-12-12
F02595–4714	NULIZ	3050008-001-002	2007-01-07–08
F03130–3119	NULIZ	3050009-001-002	2007-01-25
F03483–4704	NULIZ	3050010-001-002	2007-01-22
F08082+2521	NISIG	3610001-001	2009-10-22
F09019+5136	NISIG	3610011-001-002	2009-10-25–26
F09174+0821	NISIG	3610035-001-002	2009-11-12–13
F09395+3939	CLNSL	3350003-001-003	2009-05-05
F09501+5535	NULIZ	3050001-001-002	2006-11-01, 2007-04-29
F10035+4852	NISIG	3610008-001-002	2009-11-06–07
F10300+3509	NULIZ	3051003-001-002	2007-05-17
F10565+2448	NULIZ	3051019-001	2007-05-28
F11087+1036	CLNSL	3350028-001	2009-06-05
F11163+5707	NISIG	3610013-001-004	2009-11-14
F11213+6556	NULIZ	3050030-001	2007-05-04
F11514+1212	NULIZ	3051008-001-002	2007-06-15
F12207+6329	CLNSL	3350024-001-002	2009-05-14
F12232+5532	NULIZ	3051006-001-002	2007-05-25
F12469+4359	NULIZ	3051010-001-002	2007-06-11
F12471+4759	NULIZ	3051009-001-002	2007-06-07–08
F12479+3705	NULIZ	3051005-001-002	2007-06-16
F12536+5113	NISIG	3610028-001-004	2009-12-06–07
F13099+4627	CLNSL	3350015-001	2009-06-12
F13300+6652	CLNSL	3350025-001-008 <sup>b</sup>	2008-11-19–22, 2009-05-18–20
F13380+3339	NULIZ	3051001-001-002	2007-06-30
F14014+3718	NULIZ	3051007-001-002	2007-07-03
F14166+6514	NULIZ	3051014-001-002	2007-05-28
F14379+5420	NULIZ	3050004-001-002	2006-12-24
F14413+3730	NULIZ	3050005-001-002	2007-01-11–12
F14541+4906	NULIZ	3050006-001-002	2007-01-04
F15002+4945	NULIZ	3051015-001-002	2007-07-06
F16533+6216	CLNSL	3350023-001-002	2009-01-08
F22509–0040	CLNSL	3350036-001-002	2009-06-04
F23223+1459	CLNSL	3350037-001-005	2009-06-19–20
09022–3615	NULIZ	3051018-001-002	2007-05-26

<sup>a</sup>The 2nd pointing was not used to obtain the final spectra.

<sup>b</sup>The 4th pointing was not used to obtain the final spectra.

Table 3. Measurements and AGN signature.

Object (1)	Aper. (2)	$f_{3.3\text{PAH}}$ (3)	$\text{EW}_{3.3\text{PAH}}$ (4)	$f_{\text{Br}\alpha}$ (5)	$f_{\text{Br}\beta}$ (6)	$\tau_{3.1}$ (7)	$\tau_{3.4}$ (8)	$\Gamma$ (9)	AGN (10)
F01159–0029	8.8	$6.9 \pm 1.8$	$59 \pm 16$	$< 2.0$	$2.6 \pm 1.1$	$< 0.10$	...	$-2.72 \pm 0.07$	X
F01212–5025	10.2	$< 0.5$	$< 13$	...	$< 0.5$	$< 0.15$	$< 0.14$	$-2.06 \pm 0.06$	○
F02595–4714	8.8	$0.3 \pm 0.1$	$18 \pm 6$	...	$0.8 \pm 0.1$	$< 0.25$	$< 0.35$	$-2.13 \pm 0.07$	○
F03130–3119	8.8	$1.2 \pm 0.1$	$81 \pm 9$	...	$< 0.6$	$< 0.39$	$< 0.15$	$-2.38 \pm 0.10$	X
F03483–4704	8.8	$< 0.5$	$< 28$	...	$< 0.6$	$< 0.43$	$< 0.24$	$-1.58 \pm 0.10$	○
F08082+2521	13.1	$6.6 \pm 1.7$	$40 \pm 10$	...	...	$< 0.13$	...	$-3.11 \pm 0.08$	X
F09019+5136	10.2	$15.4 \pm 2.4$	$104 \pm 16$	$< 1.8$	$< 1.4$	$< 0.12$	...	$-2.37 \pm 0.06$	X
F09174+0821	11.7	$10.1 \pm 1.6$	$48 \pm 7$	$< 1.0$	$< 2.1$	$< 0.10$	...	$-2.66 \pm 0.05$	X
F09395+3939	7.3	$1.2 \pm 0.2$	$60 \pm 8$	$< 0.7$	$< 0.8$	$< 0.13$	...	$-2.48 \pm 0.14$	X
F09501+5535	7.3	$0.5 \pm 0.1$	$58 \pm 8$	...	$< 0.4$	$0.96 \pm 0.16$	$0.59 \pm 0.30$	$-1.00 \pm 0.09$	○
F10035+4852	8.8	$14.6 \pm 1.3$	$83 \pm 8$	$< 1.3$	$< 2.0$	$< 0.13$	...	$-2.53 \pm 0.05$	X
F10300+3509	7.3	$0.5 \pm 0.1$	$43 \pm 11$	...	$< 0.6$	$< 0.38$	...	$-2.61 \pm 0.15$	X
F10565+2448	10.2	$37.0 \pm 5.6$	$111 \pm 17$	$4.4 \pm 0.8$	$4.9 \pm 1.4$	$0.36 \pm 0.06$	...	$-2.30 \pm 0.05$	○
F11087+1036	10.2	$5.6 \pm 1.1$	$88 \pm 18$	$< 0.8$	$< 1.6$	$< 0.14$	$< 0.14$	$-3.07 \pm 0.11$	X
F11163+5707	7.3	$1.5 \pm 0.3$	$66 \pm 14$	$< 0.9$	$< 1.0$	$< 0.15$	...	$-1.97 \pm 0.15$	X
F11213+6556	7.3	$< 0.5$	$< 37$	...	$< 0.8$	$< 0.26$	$< 0.27$	$-2.26 \pm 0.16$	○
F11514+1212	5.8	$< 0.5$	$< 61$	...	$< 0.5$	$< 0.15$	...	$-4.54 \pm 0.22$	X
F12207+6329	10.2	$15.7 \pm 1.8$	$180 \pm 20$	$3.0 \pm 0.3$	$2.3 \pm 0.4$	$< 0.09$	...	$-2.79 \pm 0.08$	X
F12232+5532	8.8	$1.0 \pm 0.1$	$39 \pm 3$	...	$< 0.7$	$< 0.16$	$< 0.21$	$-1.86 \pm 0.08$	○
F12469+4359	7.3	$< 0.6$	$< 88$	...	$< 0.5$	$1.21 \pm 0.47$	...	$-3.45 \pm 0.19$	○
F12471+4759	7.3	$0.6 \pm 0.2$	$22 \pm 7$	...	$< 0.6$	$< 0.20$	$< 0.14$	$-2.01 \pm 0.07$	○
F12479+3705	7.3	$0.6 \pm 0.2$	$28 \pm 8$	...	$< 0.6$	$0.22 \pm 0.07$	$< 0.11$	$-2.53 \pm 0.10$	○
F12536+5113	7.3	$4.0 \pm 0.6$	$147 \pm 23$	$< 1.6$	$< 1.2$	$< 0.25$	...	$-2.62 \pm 0.28$	X
F13099+4627	11.7	$< 5.1$	$< 15$	$< 1.2$	$< 3.2$	$0.12 \pm 0.04$	...	$-3.20 \pm 0.05$	○
F13300+6652	7.3	$< 0.3$	$< 22$	$< 0.3$	$< 0.5$	$< 0.24$	$< 0.23$	$-2.93 \pm 0.11$	○
F13380+3339	7.3	$1.1 \pm 0.1$	$44 \pm 5$	...	$< 0.6$	$< 0.35$	$< 0.15$	$-2.16 \pm 0.08$	X
F14014+3718	7.3	$1.4 \pm 0.1$	$76 \pm 5$	...	$< 0.7$	$< 0.14$	...	$-1.68 \pm 0.08$	X
F14166+6514	5.8	$< 0.7$	$< 31$	...	$< 0.5$	$< 0.18$	...	$-2.04 \pm 0.20$	○
F14379+5420	4.4	$0.6 \pm 0.2$	$71 \pm 27$	...	$< 0.3$	$< 0.42$	...	$-1.86 \pm 0.21$	X
F14413+3730	7.3	$0.9 \pm 0.3$	$55 \pm 20$	...	$< 0.5$	$< 0.37$	$< 0.12$	$-2.54 \pm 0.14$	X
F14541+4906	8.8	$< 0.4$	$< 3$	...	$< 0.7$	$< 0.08$	$0.29 \pm 0.05$	$0.62 \pm 0.07$	○
F15002+4945	7.3	$< 0.7$	$< 3$	...	$< 0.7$	$< 0.11$	...	$-0.52 \pm 0.05$	○
F16533+6216	10.2	$6.7 \pm 0.8$	$137 \pm 16$	$0.6 \pm 0.3$	$0.4 \pm 0.2$	$0.42 \pm 0.14$	...	$-2.33 \pm 0.08$	○
F22509–0040	7.3	$17.8 \pm 1.9$	$125 \pm 15$	$3.0 \pm 1.2$	$< 2.1$	$0.62 \pm 0.19$	$0.38 \pm 0.14$	$-0.91 \pm 0.08$	○
F23223+1459	13.1	$< 1.5$	$< 3$	$< 0.9$	...	$0.23 \pm 0.06$	...	$-3.38 \pm 0.05$	○
09022–3615	13.1	$21.0 \pm 4.4$	$44 \pm 10$	$4.9 \pm 0.9$	$4.3 \pm 1.2$	$< 0.08$	$< 0.06$	$0.55 \pm 0.12$	○

Note. — Column 1: Object name in the *IRAS* catalogs. Column 2: Aperture width used for the extraction ( $''$ ). Column 3: Observed flux of the  $3.3 \mu\text{m}$  PAH emission ( $10^{-14} \text{ ergs s}^{-1} \text{ cm}^{-2}$ ). Column 4: Rest-frame equivalent width of the  $3.3 \mu\text{m}$  PAH emission (nm). Columns 5–6: Observed fluxes of  $\text{Br}\alpha$  and  $\text{Br}\beta$  ( $10^{-14} \text{ ergs s}^{-1} \text{ cm}^{-2}$ ). The  $\text{Br}\alpha$  and  $\text{Br}\beta$  fluxes of sources at  $z > 0.2$  and  $z < 0.02$  are not presented, respectively, because the measurements near the edge of the spectra are uncertain. Columns 7–8: Optical depths of the  $3.1 \mu\text{m}$   $\text{H}_2\text{O}$  ice and  $3.4 \mu\text{m}$  bare carbonaceous dust absorption features. The  $3.4 \mu\text{m}$  optical depths are not presented if they are significantly affected by the  $3.4 \mu\text{m}$  PAH sub-peak. Column 9: Continuum slope  $\Gamma$  ( $F_\lambda \propto \lambda^\Gamma$ ). Column 10: AGN signature from the NIR features ( $\text{EW}_{3.3\text{PAH}} < 40 \text{ nm}$ ,  $\tau_{3.1} > 0.3$ ,  $\tau_{3.4} > 0.2$ , or  $\Gamma > -1$ ).

Table 4. NIR AGN detection rate in bins of optical spectral type and of infrared luminosity.

Sample	$\log L_{\text{IR}}$ ( $L_{\odot}$ )	Optical spectral type					
		Star-forming	Composite	LINER	Seyfert 2	Seyfert 1	Unclassified
This study	12.3–13.0	100% (1/1)	100% (3/3)	... (0/0)	50% (1/2)	100% (1/1)	0% (0/1)
	12.0–12.3	50% (2/4)	60% (3/5)	... (0/0)	... (0/0)	... (0/0)	50% (2/4)
	11.0–12.0	0% (0/3)	50% (3/6)	... (0/0)	100% (1/1)	... (0/0)	... (0/0)
	10.0–11.0	0% (0/3)	... (0/0)	100% (2/2)	... (0/0)	... (0/0)	... (0/0)
Imanishi+08,10	12.3–13.0	100% (2/2)	77% (10/13)	... (0/0)	75% (6/8)	... (0/0)	0% (0/2)
	12.0–12.3	67% (4/6)	61% (19/31)	50% (1/2)	70% (14/20)	... (0/0)	57% (4/7)
	11.0–12.0	18% (3/17)	25% (5/20)	... (0/0)	50% (5/10)	100% (1/1)	20% (2/10)

Note. — The values in parentheses mean the number of sources with AGN signature/total number of sources in each bin from our sample and the sample in Imanishi et al. (2008, 2010a). The optical spectral types of the Imanishi sample are taken from Yuan et al. (2010) so that the same criteria of Kewley et al. (2006) are used for the two samples. For sources with multiple nuclei, if AGN signatures are seen at least in one nucleus, then these sources are considered to be AGN. For an unbiased comparison, the additional interesting sources in the Imanishi sample are not included.